RESEARCH ARTICLE SUMMARY

PSYCHENCODE2

A data-driven single-cell and spatial transcriptomic map of the human prefrontal cortex

Louise A. Huuki-Myers, Abby Spangler, Nicholas J. Eagles, Kelsey D. Montgomery, Sang Ho Kwon, Boyi Guo, Melissa Grant-Peters, Heena R. Divecha, Madhavi Tippani, Chaichontat Sriworarat, Annie B. Nguyen, Prashanthi Ravichandran, Matthew N. Tran, Arta Seyedian, PsychENCODE Consortium†, Thomas M. Hyde, Joel E. Kleinman, Alexis Battle, Stephanie C. Page, Mina Ryten, Stephanie C. Hicks, Keri Martinowich, Leonardo Collado-Torres*, Kristen R. Maynard*

INTRODUCTION: The cortical layers of the human neocortex were classically defined by histological distinction of cell types according to size, shape, and density. However, emerging single-cell and spatially resolved transcriptomic technologies have facilitated the identification of molecularly defined cell populations and spatial domains that move beyond classic cell type definitions and cytoarchitectural boundaries.

RATIONALE: Given the close relationship between brain structure and function, assigning gene expression to distinct anatomical subdivisions and cell populations within the human brain improves our understanding of these highly specialized regions and how they contribute to brain disorders. We sought to create a data-driven molecular neuroanatomical map of the human dorsolateral prefrontal cortex (DLPFC) at cellular resolution using unsupervised transcriptomic approaches to identify spatial domains associated with neuropsychiatric and neurodevelopmental disorders.

RESULTS: We generated complementary single-cell and spatial transcriptomic data from 10 adult, neurotypical control donors across the anterior-posterior axis of the DLPFC. Unsupervised spatial clustering revealed fine-resolution data-driven spatial domains with distinct molecular signatures, including deep cortical sublayers and a vasculature-enriched meninges layer. Cell type clustering of single-nucleus RNA-sequencing (snRNA-seq) data revealed 29 distinct populations across seven broad neuronal and glial cell types, including 15 excitatory subpopulations. To add cellular resolution to our data-driven molecular atlas, we took two complementary approaches to integrate single-cell and spatial transcriptomics data. First, we used our previously developed spatial registration framework to map the paired snRNA-seq data to specific unsupervised spatial domains, providing anatomy-based laminar identities to excitatory neuron subpopulations. Second, we used three existing spot-level deconvolution tools to computationally predict the cell type composition of spatial domains on the basis of the paired snRNA-seq reference data. These tools were rigorously benchmarked against a newly generated gold-standard reference dataset acquired with the Visium Spatial Proteogenomics assay, which enabled us to label and quantify four broad cell types across the DLPFC on the basis of protein marker expression, including neurons, oligodendrocytes, astrocytes, and microglia. Using these approaches, we identified the proportion of cell types in each spatial domain and showed that these proportions were consistent across individuals and the DLPFC anterior-posterior axis. We demonstrated the clinical relevance of our highly integrated molecular atlas using cell-cell communication analyses to spatially map cell type–specific ligand-receptor interactions associated with genetic risk for schizophrenia (SCZ). For example, we mapped the interaction between ephrin ligand EFNA5 and ephrin receptor EPHA5 to deep-layer excitatory neuron subtypes and spatial domains. To leverage the rich single-cell data generated by PsychENCODE Consortium companion studies, we spatially registered eight DLPFC snRNA-seq datasets collected across the consortium in the context of different neuropsychiatric disorders and demonstrated a convergence of excitatory, inhibitory, and non-neuronal cell types in relevant spatial domains. Using PsychENCODE Consortium and other publicly available gene sets, we further demonstrated the clinical relevance of our data-driven molecular atlas by mapping the enrichment of cell types and genes associated with neuropsychiatric disorders—including autism spectrum disorder, posttraumatic stress disorder, and major depressive disorder—to discrete spatial domains.

CONCLUSION: Our study identified high-resolution, data-driven spatial domains across the human DLPFC, providing anatomical context for cell type–specific gene expression changes associated with neurodevelopmental disorders and psychiatric illness. We provide a roadmap for the implementation and biological validation of unsupervised spatial clustering approaches in other regions of the human brain. We share interactive data resources for the scientific community to further interrogate molecular mechanisms associated with complex brain disorders. ■

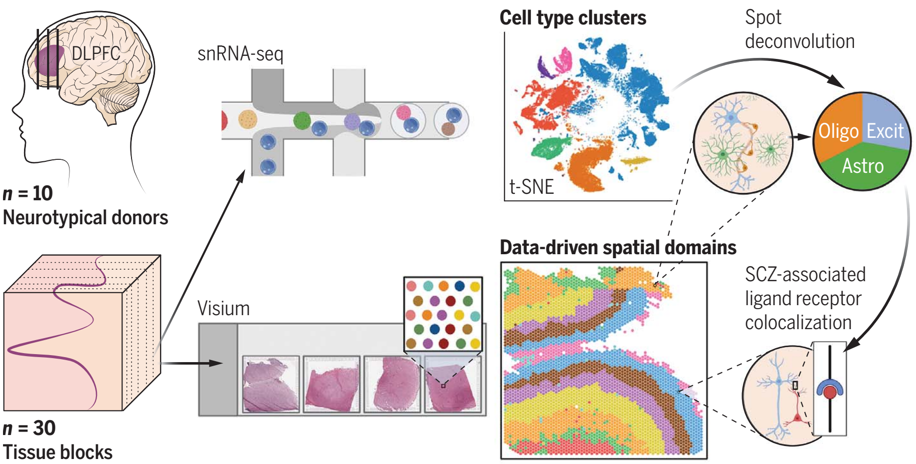

Data-driven molecular anatomy of the human DLPFC. Integrated single-nucleus and spatial transcriptomics data were generated across the anterior-posterior axis of the human DLPFC from 10 neurotypical control donors to create a data-driven molecular neuroanatomical atlas of the neocortex identifying spatial domains. Integrative analyses revealed distinct cell type compositions, cell-cell interactions, and colocalization of ligand-receptor pairs linked to schizophrenia genetic risk. t-SNE, *t*-distributed stochastic neighbor embedding. [Created with BioRender.com.]

The list of author affiliations is available in the full article online.
*Corresponding author. Email: kristen.maynard@libd.org (K.R.M.); lcolladotor@gmail.com (L.C.-T.)
†PsychENCODE Consortium collaborators and affiliations are listed in the supplementary materials.

Cite this article as L. A. Huuki-Myers *et al.*, *Science* 384, eadh1938 (2024). DOI: 10.1126/science.adh1938

READ THE FULL ARTICLE AT
https://doi.org/10.1126/science.adh1938

RESEARCH ARTICLE

PSYCHENCODE2

A data-driven single-cell and spatial transcriptomic map of the human prefrontal cortex

Louise A. Huuki-Myers[1], Abby Spangler[1], Nicholas J. Eagles[1], Kelsey D. Montgomery[1], Sang Ho Kwon[1,2], Boyi Guo[3], Melissa Grant-Peters[4,5], Heena R. Divecha[1], Madhavi Tippani[1], Chaichontat Sriworarat[1,2], Annie B. Nguyen[1], Prashanthi Ravichandran[6], Matthew N. Tran[1], Arta Seyedian[1], PsychENCODE Consortium†, Thomas M. Hyde[1,7,8], Joel E. Kleinman[1,7], Alexis Battle[6,9,10,11], Stephanie C. Page[1,7], Mina Ryten[4,5,12], Stephanie C. Hicks[3,6,11,13], Keri Martinowich[1,2,7,14], Leonardo Collado-Torres[1,3,13]*, Kristen R. Maynard[1,2,7]*

The molecular organization of the human neocortex historically has been studied in the context of its histological layers. However, emerging spatial transcriptomic technologies have enabled unbiased identification of transcriptionally defined spatial domains that move beyond classic cytoarchitecture. We used the Visium spatial gene expression platform to generate a data-driven molecular neuroanatomical atlas across the anterior-posterior axis of the human dorsolateral prefrontal cortex. Integration with paired single-nucleus RNA-sequencing data revealed distinct cell type compositions and cell-cell interactions across spatial domains. Using PsychENCODE and publicly available data, we mapped the enrichment of cell types and genes associated with neuropsychiatric disorders to discrete spatial domains.

The emergence of single-cell and spatially resolved transcriptomics has facilitated the generation of integrated molecular anatomical maps across a variety of tissues in both rodents and humans (1–4). Data-driven unsupervised approaches to identify spatial domains (SpDs) in these large datasets, particularly in the rodent brain, have refined our understanding of the spatial organization of tissues beyond classical cytoarchitectural boundaries (2), and computational models have helped to reveal new insights into cellular diversification during development (5). However, efforts to generate spatially resolved transcriptomics data in the human brain at the scale and size necessary to use these approaches with sufficient statistical power have lagged behind.

We previously characterized the spatial topography of gene expression in the human dorsolateral prefrontal cortex (DLPFC), a brain region associated with several neurodevelopmental and psychiatric disorders (6–11), by manually annotating the six histological layers and white matter (WM) of the neocortex in a small cohort of three neurotypical adult donors (12). Although we identified robust layer-enriched gene expression with this approach, recent computational tools for unsupervised clustering (13–17) and cell-to-cell communication (CCC) (18) combined with the ability to expand the generation of molecular neuroanatomical maps across a larger donor pool has enabled data-driven identification of higher-resolution SpDs. Applying these data-driven approaches to larger-scale studies may facilitate the demarcation of fine cortical sublayers, which currently lack molecular annotations. They also could enable identification of nonlaminar SpDs associated with anatomical or topographical features in the human brain, including vasculature. In this work, we sought to develop and validate a framework for the application of unsupervised spatial clustering approaches in human brain tissue across different anterior-posterior positions of the DLPFC and generate an analytical roadmap that can be extended to other brain areas with less well-characterized neuroanatomical architecture in the future.

Recent single-nucleus RNA-sequencing (snRNA-seq) analyses are defining transcriptionally distinct DLPFC cell types and revealing cell type–specific changes associated with neurodevelopmental and neuropsychiatric disorders, such as schizophrenia (SCZ), autism spectrum disorder (ASD), major depressive disorder (MDD), and posttraumatic stress disorder (PTSD) (19–23). However, snRNA-seq data lack spatial context, which when retained during molecular profiling can provide important insights into CCC and disease pathogenesis. To facilitate this type of analysis, we generated large-scale, unsupervised spatial transcriptomic molecular maps of the human DLPFC from 10 neurotypical brain donors, which we integrated with snRNA-seq data across a variety of brain disorders. This spatially resolved, molecular atlas of gene expression architecture in the human brain is provided as an interactive data resource for the scientific community to help reveal molecular mechanisms associated with psychiatric illness.

Study overview

We applied single-cell and spatial transcriptomic approaches to create a large-scale, data-driven spatial map of gene expression at single-cell resolution in the adult human DLPFC to identify SpDs, define CCC patterns, and perform spatial registration of cell types across brain disorders (Fig. 1, A and B, and fig. S1). Using the Visium spatial transcriptomics platform (24), we measured spatial gene expression in fresh frozen post-mortem human tissue blocks from 10 neurotypical adult donors (table S1) in three positions spanning the rostral-caudal axis of the DLPFC [anterior (Ant), middle (Mid), and posterior (Post)] for a total of 30 tissue sections [$n = 10$ tissue sections per position] (Fig. 1A). In parallel, we performed snRNA-seq (10x Genomics 3′ gene expression) on a subset of the same DLPFC samples ($n = 1$ or 2 blocks per donor) to generate matched snRNA-seq and spatial transcriptomic data for 19 tissue blocks (Fig. 1, A to C). To preserve layer 1 (L1), blocks were microdissected across sulci in the plane perpendicular to the pia that extended to the gray matter–WM junction. The morphology of each tissue block was assessed with RNAscope multiplex single-molecule fluorescent in situ hybridization (smFISH), using regional and laminar marker genes to ensure dissection consistency (Fig. 1D). Sample orientation was confirmed through expression of genes enriched in the gray matter (*SNAP25*), WM (*MBP*), and L5 (*PCP4*) (Fig. 1D and figs. S2 to S4). For Visium, 4866 (4.1%) spots with low library size were excluded (fig. S5), resulting in a total of 113,927 spots across 30 tissue blocks and 10 donors. Downstream analyses at the gene level (fig. S6) and spot level (figs. S7 and S8) were not affected by tissue artifacts, including wrinkles, shears, and folds [supplementary materials (SM), materials and methods, “Evaluating the impact

---

[1]Lieber Institute for Brain Development, Johns Hopkins Medical Campus, Baltimore, MD 21205, USA. [2]The Solomon H. Snyder Department of Neuroscience, Johns Hopkins School of Medicine, Baltimore, MD 21205, USA. [3]Department of Biostatistics, Johns Hopkins Bloomberg School of Public Health, Baltimore, MD 21205, USA. [4]Genetics and Genomic Medicine, Great Ormond Street Institute of Child Health, University College London, London WC1N 1EH, UK. [5]Aligning Science Across Parkinson’s (ASAP) Collaborative Research Network, Chevy Chase, MD 20815, USA. [6]Department of Biomedical Engineering, Johns Hopkins School of Medicine, Baltimore, MD 21218, USA. [7]Department of Psychiatry and Behavioral Sciences, Johns Hopkins School of Medicine, Baltimore, MD 21205, USA. [8]Department of Neurology, Johns Hopkins School of Medicine, Baltimore, MD 21205, USA. [9]Department of Computer Science, Johns Hopkins University, Baltimore, MD 21218, USA. [10]Department of Genetic Medicine, Johns Hopkins School of Medicine, Baltimore, MD 21205, USA. [11]Malone Center for Engineering in Healthcare, Johns Hopkins University, Baltimore, MD 21218, USA. [12]NIHR Great Ormond Street Hospital Biomedical Research Centre, University College London, London WC1N 1EH, UK. [13]Center for Computational Biology, Johns Hopkins University, Baltimore, MD 21205, USA. [14]Johns Hopkins Kavli Neuroscience Discovery Institute, Johns Hopkins University, Baltimore, MD 21218, USA.

***Corresponding author. Email: kristen.maynard@libd.org (K.R.M.); lcolladotor@gmail.com (L.C.-T.)**

†PsychENCODE Consortium collaborators and affiliations are listed in the supplementary materials.

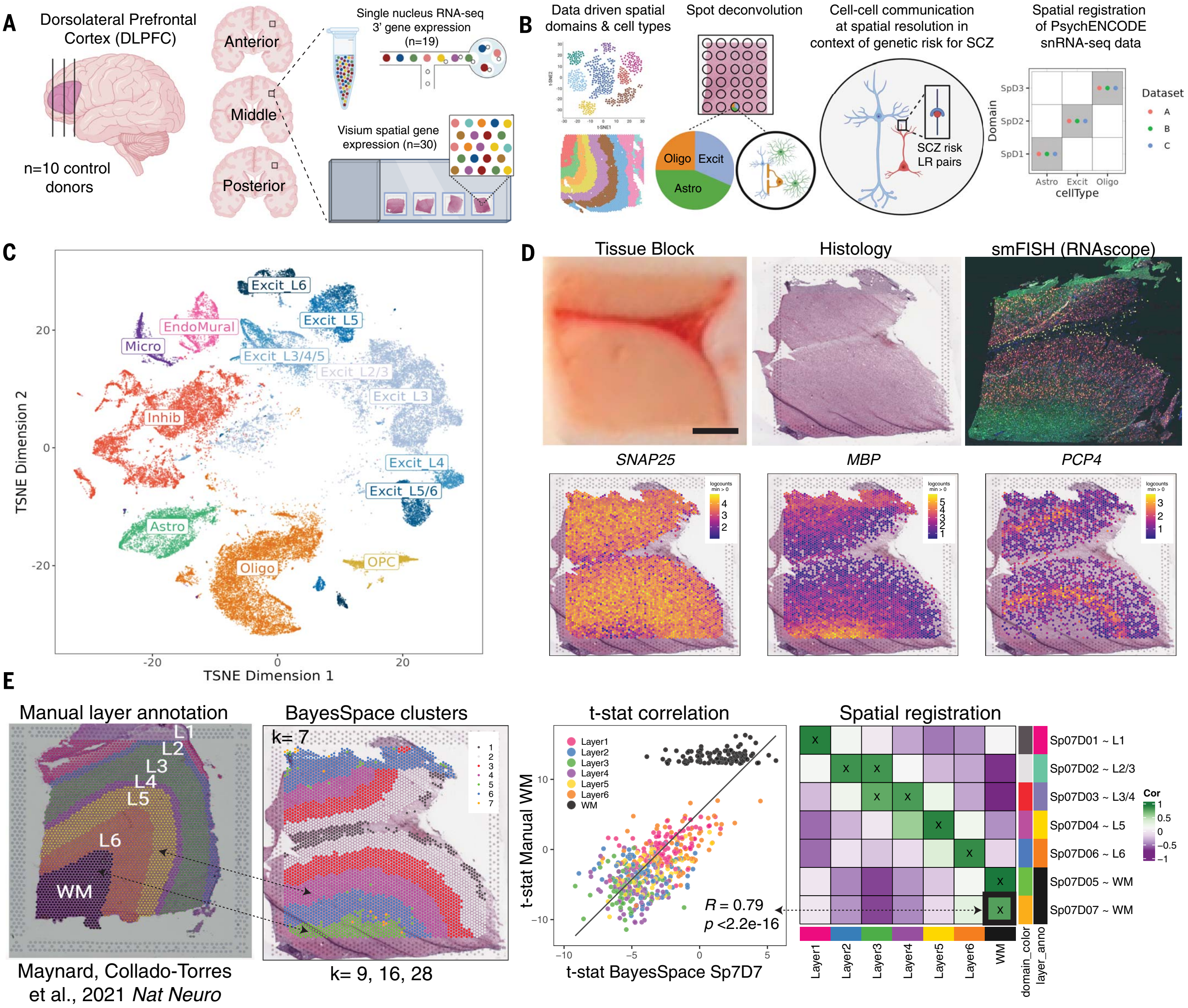

Fig. 1. Study design to generate paired snRNA-seq and spatially resolved transcriptomic data across DLPFC. (**A**) DLPFC tissue blocks were dissected across the rostral-caudal axis from 10 adult neurotypical control post-mortem human brains, including anterior (Ant), middle (Mid), and posterior (Post) positions (n = 3 blocks per donor, n = 30 blocks total). The same tissue blocks were used for snRNA-seq (10x Genomics 3′ gene expression assay, n = 1 to 2 blocks per donor, n = 19 samples) and spatial transcriptomics (10x Genomics Visium spatial gene expression assay, n = 3 blocks per donor, n = 30 samples) (fig. S1). (**B**) Paired snRNA-seq and Visium data were used to identify data-driven SpDs and cell types, perform spot deconvolution, conduct CCC analyses, and spatially register companion PsychENCODE snRNA-seq DLPFC data. (**C**) t-distributed stochastic neighbor embedding (t-SNE) summarizing layer-resolution cell types identified with snRNA-seq. (**D**) Tissue block orientation and morphology was confirmed with H&E staining and single-molecule fluorescent in situ hybridization (smFISH) with RNAscope (*SLC17A7* marking excitatory neurons in pink, *MBP* marking WM in green, *RELN* marking L1 in yellow, and *NR4A2* marking L6 in orange). Scale bar, 2 mm. Spotplots depicting log-transformed normalized expression (logcounts) of *SNAP25*, *MBP*, and *PCP4* in the Visium data confirm the presence of gray matter, WM, and cortical layers, respectively (figs. S2 to S4). (**E**) Schematic of unsupervised SpD identification and registration by using *BayesSpace* SpDs at k = 7. Enrichment t-statistics computed on *BayesSpace* SpDs were correlated with manual histological layer annotations from (12) to map SpDs to known histological layers. The heatmap of correlation values summarizes the relationship between *BayesSpace* SpDs and classic histological layers. Higher-confidence annotations (cor > 0.25, merge ratio = 0.1) (SM, "Spatial registration of *Spatial Domains*") are indicated with an "X."

of histology artifacts on Visium H&E data"]. For snRNA-seq, 54,394 nuclei across 19 tissue blocks from 10 donors passed quality control and were included in the study (Fig. 1C). Using these integrated datasets, we performed several analyses, including unsupervised clustering, spot deconvolution, CCC analyses, and spatial registration of PsychENCODE Consortium (PEC) single-cell datasets (Fig. 1B).

Identification of data-driven SpDs at different resolutions across DLPFC

We selected an unsupervised clustering method for robust identification of laminar SpDs in Visium data by benchmarking three algorithms, graph-based clustering, *SpaGGN*, and *BayesSpace* (13, 15, 25, 26) using our previously published DLPFC Visium data [12 sections from three donors (12)]. We compared data-driven clustering accuracy against manual layer annotations (figs. S9 and S10). Among the algorithms tested, *BayesSpace* most accurately identified SpDs consistent with the histological cortical layers. Therefore, we used this clustering algorithm to identify seven unsupervised SpDs approximating the six cortical layers and WM. To relate unsupervised SpDs to the classic histological layers, we pseudo-bulked spots (by gene, sum the expression for all spots in the same SpD in a given sample) within each SpD across individual tissue sections to generate SpD-specific expression profiles and performed differential expression (DE) analysis to identify genes enriched in each SpD. Next, we performed “spatial registration” by correlating the enrichment statistics computed on *BayesSpace* SpDs with those from manually annotated cortical layers (12) to approximate the most strongly associated histological layer for a given *BayesSpace* SpD (Fig. 1E). We annotated the association of a specific SpD at cluster resolution *k* to a classic histological layer using the term $\mathrm{Sp_kD_d} \sim L$, where *L* refers to the histological layer most strongly associated to domain *d* after cluster registration at resolution *k*. For example, SpD 7 at cluster resolution $k = 7$ ($\mathrm{Sp_7D_7}$) was mostly strongly associated with WM (Fig. 1E) and is annotated as $\mathrm{Sp_7D_7} \sim$ WM. We found that $k = 7$ was not sufficient to fully separate histological layers, especially superficial L2 to L4, suggesting the presence of higher-resolution data-driven SpDs and highlighting the challenges of manually annotating SpDs (12).

We next evaluated how increasing cluster resolution (k) influenced the identification and cluster registration of unsupervised SpDs (Fig. 2). As expected, clustering at $k = 2$ reliably separated WM and gray matter (figs. S11 and S12). Next, we evaluated three clustering resolutions: a broad-resolution $k = 9$, a data-driven fine-resolution $k = 16$ (figs. S13 and S14), and a superfine-resolution $k = 28$. Hereafter, we refer to these SpDs as $\mathrm{Sp_9D}$, $\mathrm{Sp_{16}D}$, and $\mathrm{Sp_{28}D}$, respectively. Broad clustering most accurately recapitulated the classic histological layers with clear separation of $\mathrm{Sp_9Ds}$ enriched in genes expressed in L1 to L6 and WM (Fig. 2, A and B, and fig. S15). At fine clustering resolution, SpDs were largely laminar, with two or more $\mathrm{Sp_{16}Ds}$ registering to a given histological layer, which suggests the presence of molecularly defined sublayers (Fig. 2, A and B, and fig. S16). At superfine resolution, many SpDs lacked a laminar structure, but spots belonging to $\mathrm{Sp_{28}Ds}$ frequently mapped back to a single broad or fine-resolution SpD (figs. S17 and S18). To evaluate the unsupervised architecture of cortical layers in the human DLPFC in more depth, we focused on broad and fine SpDs on the basis of the robust laminar features of these domains.

Enrichment of differentially expressed genes in unsupervised SpDs

To identify the molecular signatures of SpDs within each clustering resolution, we next performed DE analysis with linear mixed-effects modeling using the $\mathrm{Sp_9D}$- or $\mathrm{Sp_{16}D}$-specific expression profiles. As previously described, we used three different statistical models: an analysis of variance (ANOVA) model, an enrichment model, and a pairwise model (12). As expected, all three models confirmed that unsupervised clustering at broad or fine resolution identified biologically meaningful SpDs with significant DE of genes across the laminar architecture of the cortex [5931 false discovery rate (FDR) < 5% distinct enriched genes in at least one $\mathrm{Sp_9D}$] (SM materials and methods, “Layer-level data processing and differential expression modeling”). Although we did identify 512 distinct genes that were differentially enriched across the anterior-posterior axis of the DLPFC, SpD had a much stronger effect on gene expression as compared with anatomical position (anterior, middle, or posterior) (fig. S19).

Analysis of differentially expressed genes (DEGs) identified by using the enrichment model allowed for characterization of previously unrecognized data-driven SpDs, such as $\mathrm{Sp_9D_1}$ and $\mathrm{Sp_{16}D_1}$ (Fig. 2B). At both $k = 9$ and $k = 16$, domain 1 is adjacent to histological L1 and enriched for genes associated with blood vessels and brain vasculature, such as *CLDN5* ($P = 2.04 \times 10^{-75}$) (Fig. 2, C and D). Because of its thinness, this vascular-rich meninges layer was not manually annotated in our previous study (12), demonstrating the utility of unsupervised approaches to robustly identify biologically meaningful SpDs. Data-driven clustering at fine resolution also revealed molecularly defined sublayers, including two adjacent laminar spatial subdomains ($\mathrm{Sp_{16}D_{14}} \sim$ L1 and $\mathrm{Sp_{16}D_2} \sim$ L1) (Fig. 2E) enriched in L1 marker genes, including *RELN* ($P = 6.98\times 10^{-17}$, $P = 3.19 \times 10^{-19}$, respectively) and *AQP4* ($P = 9.37 \times 10^{-21}$, $P = 9.43 \times 10^{-12}$, respectively). Pairwise tests across these L1-related subdomains highlighted DE of *SPARC* (enriched in $\mathrm{Sp_{16}D_{14}} \sim$ L1, $P = 7.61 \times 10^{-14}$) and *HTRA1* (enriched in $\mathrm{Sp_{16}D_2}$~L1, $P = 1.26 \times 10^{-7}$), and principal components analysis (PCA) further confirmed the distinctive nature of these molecularly defined sublayers (Fig. 2, E to G). We also identified multiple SpDs associated with histological L4 ($\mathrm{Sp_{16}D_5}$-L4 and $\mathrm{Sp_{16}D_9}$-L4), L5 ($\mathrm{Sp_{16}D_4}$-L5 and $\mathrm{Sp_{16}D_{16}}$-L5), and L6 ($\mathrm{Sp_{16}D_7}$-L6 and $\mathrm{Sp_{16}D_{12}}$-L6) (Fig. 2B). Taken together, this analysis validated the biological relevance of data-driven SpDs and increased the understanding of the molecular neuroanatomy across the laminar architecture of the adult human DLPFC.

Identification of molecularly and spatially distinct neuronal populations across cortical layers

To add single-cell resolution to our molecular maps, we performed snRNA-seq on a subset of the same tissue blocks used for Visium (Fig. 1 and fig. S1). After assessment of quality-control metrics (figs. S20 and S21), we performed batch correction (figs. S22 to S24) and data-driven clustering to generate 29 fine-resolution clusters across seven broad cell types represented throughout the anterior-posterior DLPFC axis (Fig. 3A and fig. S25). Further, we spatially registered all clusters to the histological layers using manually annotated Visium data from previous work (Fig. 3B) (12). Given that molecularly defined excitatory neuron populations in the cortex have distinct laminar identities (27), we systematically assigned a histological layer to excitatory neuron clusters (table S2), resulting in the identification of 13 layer-resolution clusters with distinct marker genes (Fig. 3, B to D, and fig. S26). At both fine resolution and layer resolution, our clusters strongly correlated with those derived from the reference-based mapping tool Azimuth (https://azimuth.hubmapconsortium.org) (fig. S27) (28, 29).

To gain further insight into the relationship between our snRNA-seq clusters and Visium unsupervised SpDs, we performed spatial registration of fine-resolution snRNA-seq clusters with Visium SpDs at $k = 9$ and $k = 16$ (Fig. 3B). We refined the spatial positioning of our 29 fine-resolution snRNA-seq clusters and validated the laminar associations of broad and fine unsupervised SpDs. For example, we showed that snRNA-seq excitatory neuron clusters Excit_06 and Excit_08, which spatially registered to histological L6, were also highly correlated with Visium $\mathrm{Sp_9D_7}$, a domain enriched for L6-associated genes (Fig. 2B). These snRNA-seq clusters were also highly correlated with a single SpD ($\mathrm{Sp_{16}D_7}$), further refining their anatomical position to upper L6. Inhibitory γ-aminobutyric acid (GABA)–expressing populations were also assigned to specific spatial locations. For example, Inhib_05 specifically registered to histological L2, which was confirmed with strong correlations to $\mathrm{Sp_9D_3}$ and $\mathrm{Sp_{16}D_8}$ showing enrichment for L2-associated genes (Fig. 2B). We also showed registration of snRNA-seq endothelial cell populations to vascular SpDs ($\mathrm{Sp_9D_1}$ and $\mathrm{Sp_{16}D_1}$) enriched in *HBA1* and *CLDN5*. Whereas endothelial cells showed the strongest correlation with vascular-associated SpDs and glial cells showed the strongest correlation with L1- and WM-associated SpDs (Fig. 2B), these cell types are indeed distributed across the cortical layers, necessitating higher-resolution spatial mapping approaches such as spot deconvolution.

Defining cell type composition of unsupervised SpDs using spot deconvolution

Given that individual Visium spots in the human DLPFC contain an average of three cells per spot (12), we used our paired snRNA-seq data to perform cellular deconvolution of Visium spots to better understand the cell type composition of unsupervised SpDs. First, we benchmarked three spot-level deconvolution algorithms—*SPOTlight*, *Tangram*, and *Cell2location* (14, 30, 31)—using

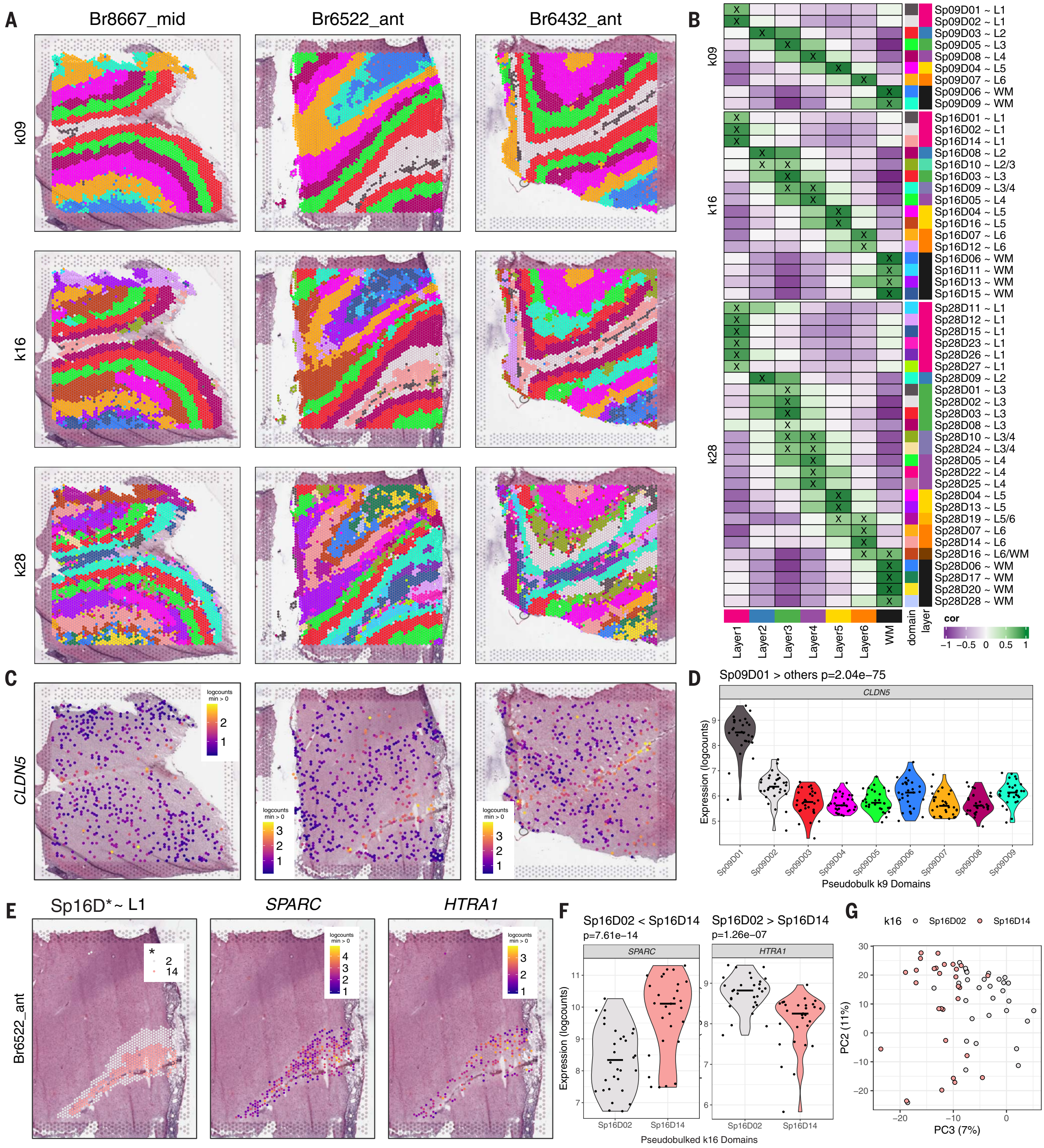

Fig. 2. Unsupervised clustering at different resolutions identifying SpDs and defining molecular anatomy of DLPFC. (**A**) *BayesSpace* clustering at *k* = 9, 16, and 28 (broad, fine, and superfine resolution, respectively, which we refer to as $\mathrm{Sp}_k\mathrm{D}_d$ for domain *d* from SpDs at *k* resolution) for three representative DLPFC tissue sections (Br8667_mid, Br6522_ant, and Br6432_ant). (**B**) Heatmap of spatial registration with manually annotated histological layers from (*12*). *BayesSpace* identifies laminar SpDs at increasing *k* with the majority of $\mathrm{Sp}_k\mathrm{D}$s correlating with one or more histological layer(s). SpDs were assigned layer annotations following spatial registration to histological layers. Annotations with high confidence (cor > 0.25, merge ratio = 0.1) (SM, "Spatial registration of *Spatial Domains*") are indicated with an "X," and this histological layer association is denoted for a given $\mathrm{Sp}_k\mathrm{D}_d$ by adding "~*L*," where *L* is the most strongly correlated histological layer (or WM) (figs. S11 to S18. (**C**) Spotplots depicting expression of *CLDN5* in vasculature domain 1 at *k* = 9 resolution ($\mathrm{Sp}_9\mathrm{D}_1$). (**D**) Violin plot confirming enrichment of *CLDN5* in $\mathrm{Sp}_9\mathrm{D}_1$ compared with other $\mathrm{Sp}_9\mathrm{D}$s across 30 tissue sections. (**E**) Spotplots of representative section Br6522_ant showing identification of molecularly defined sublayers for histological L1 at *k* = 16 ($\mathrm{Sp}_{16}\mathrm{D}_2$ and $\mathrm{Sp}_{16}\mathrm{D}_{14}$) and enrichment of *HTRA1* and *SPARC*, respectively. (**F**) Boxplots quantifying enrichment of *SPARC* and *HTRA1* in $\mathrm{Sp}_{16}\mathrm{D}_{14}$ and $\mathrm{Sp}_{16}\mathrm{D}_2$, respectively, across 30 tissue sections. (**G**) PCA plot showing separation of $\mathrm{Sp}_{16}\mathrm{D}_2$ and $\mathrm{Sp}_{16}\mathrm{D}_{14}$, supporting identification of molecularly distinct SpDs.

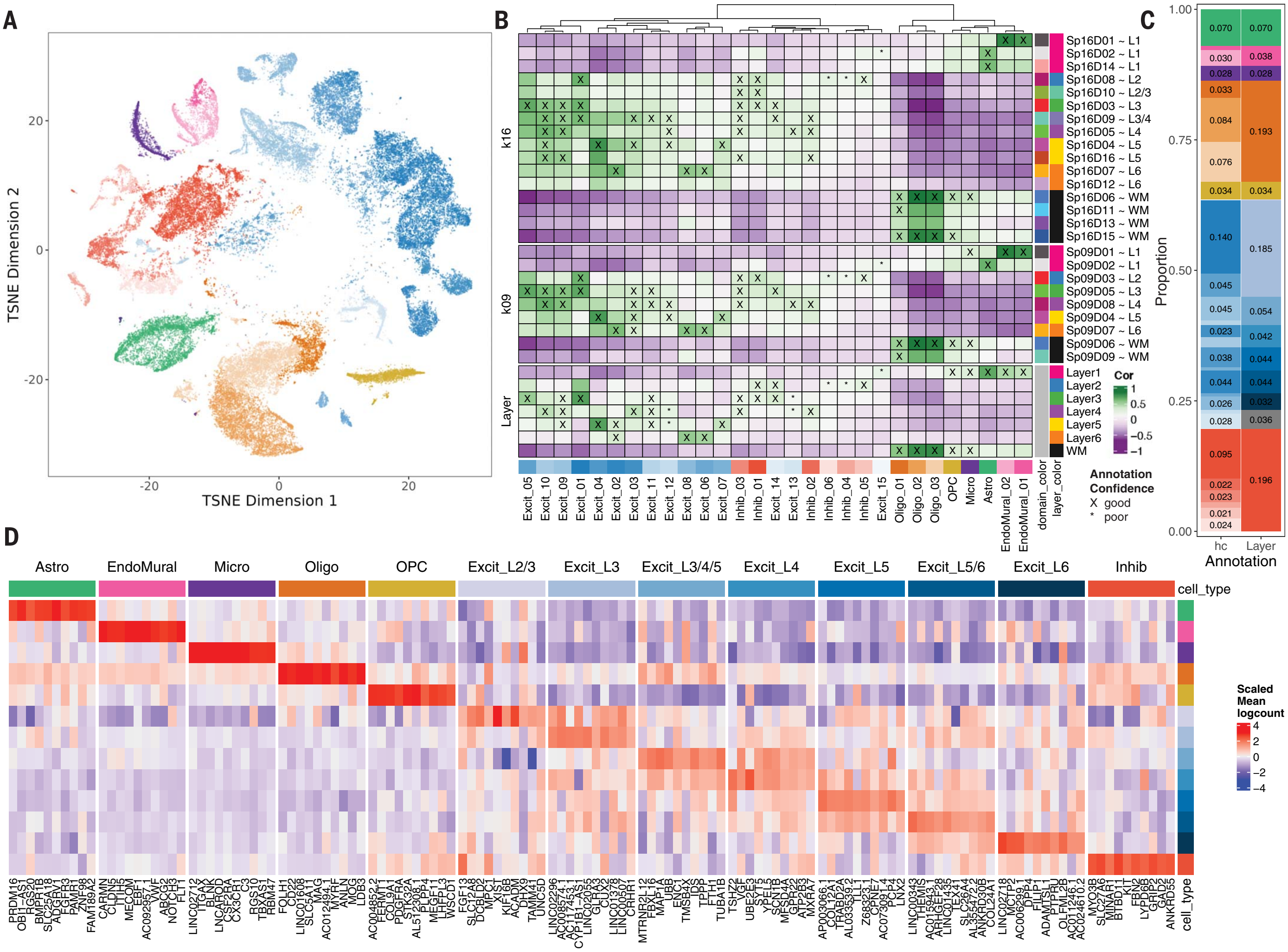

Fig. 3. Spatial registration of fine-resolution snRNA-seq clusters defining laminar cell types. (**A**) *t*-SNE plot of 56,447 nuclei across 29 cell type–annotated fine-resolution hierarchical clusters (hc; related to fig. S25A). (**B**) Spatial registration heatmap showing correlation between snRNA-seq hierarchical clusters (hc) and manually annotated histological layers from (*12*) as well as unsupervised *BayesSpace* clusters at $k = 9$ and 16 (Sp$_9$Ds and Sp$_{16}$Ds, respectively). Hierarchical clusters for excitatory neurons (Excit) were assigned layer-level annotations following spatial registration to histological layers (cor > 0.25, merge ratio = 0.25) (SM, "snRNA-seq spatial registration"). For Sp$_9$Ds and Sp$_{16}$Ds, annotations with good confidence (cor > 0.25, merge ratio = 0.1) are indicated with "X," and annotations with poor confidence are indicated with an asterisk. (**C**) Summary barplot of cell type composition for hc and layer-level resolutions (related to figs. S25B and S26) (**D**) Heatmap of the scaled mean pseudo-bulked logcounts for the top 10 marker genes identified for each cell type at layer-level resolution.

a gold-standard reference dataset acquired with the Visium Spatial Proteogenomics (Visium-SPG) assay. Visium-SPG replaces hematoxylin and eosin (H&E) histology with immunofluorescence staining, enabling us to label and quantify four broad cell types across the DLPFC, including NeuN (neurons), OLIG2 (oligodendrocytes), GFAP (astrocytes), and TMEM119 (microglia) (Fig. 4A and fig. S28). After verifying marker genes for each snRNA-seq cluster (fig. S29) and confirming the utility of these genes for spot deconvolution (Fig. 4B and figs. S30 to S32), we applied *SPOTlight*, *Tangram*, and *Cell2location* to our Visium-SPG data and calculated the predicted cell type counts per spot at broad and fine resolution (Fig. 4B and fig. S33).

To quantify algorithm performance, we took two complementary approaches: (i) evaluating the localization of laminar cell types to their expected cortical layer (Fig. 4C and figs. S34 and S35) and (ii) comparing predicted cell type counts to those obtained from immunofluorescent images by using a classification and regression tree (CART) strategy to categorize nuclei into the four immunolabeled cell types (Fig. 4D and figs. S36 to S39). Using the first approach, we found that *Tangram* and *Cell2location* performed best across all cell types, but *SPOTlight* failed to accurately map excitatory neuron subtypes to the correct layer (Fig. 4B). Using the second approach, we found that the predicted counts from *Tangram* and *Cell2location* also had the highest correlation to CART-calculated counts (Fig. 4D), and *Tangram* showed the most consistent performance at both broad and layer-level resolution across all cell types and samples (Fig. 4E). Last, we applied *Tangram* and *Cell2location* to our H&E Visium dataset to predict the cellular composition of SpDs across the anterior-posterior axis of the DLPFC (Fig. 4, F and G, and figs. S40 and S41) and found that *Tangram* and *Cell2location* showed differences in the predicted cell counts per spot (Fig. 4F), whereas for both tools, the predicted cellular composition of SpDs was consistent across samples at both broad ($k = 9$) and fine ($k = 16$) resolution regardless of DLPFC position (anterior, middle, or posterior).

Spatial mapping of ligand-receptor interactions associated with SCZ

To add clinical relevance to this integrated DLPFC dataset, we next sought to identify interacting cell types and spatially map ligand-receptor

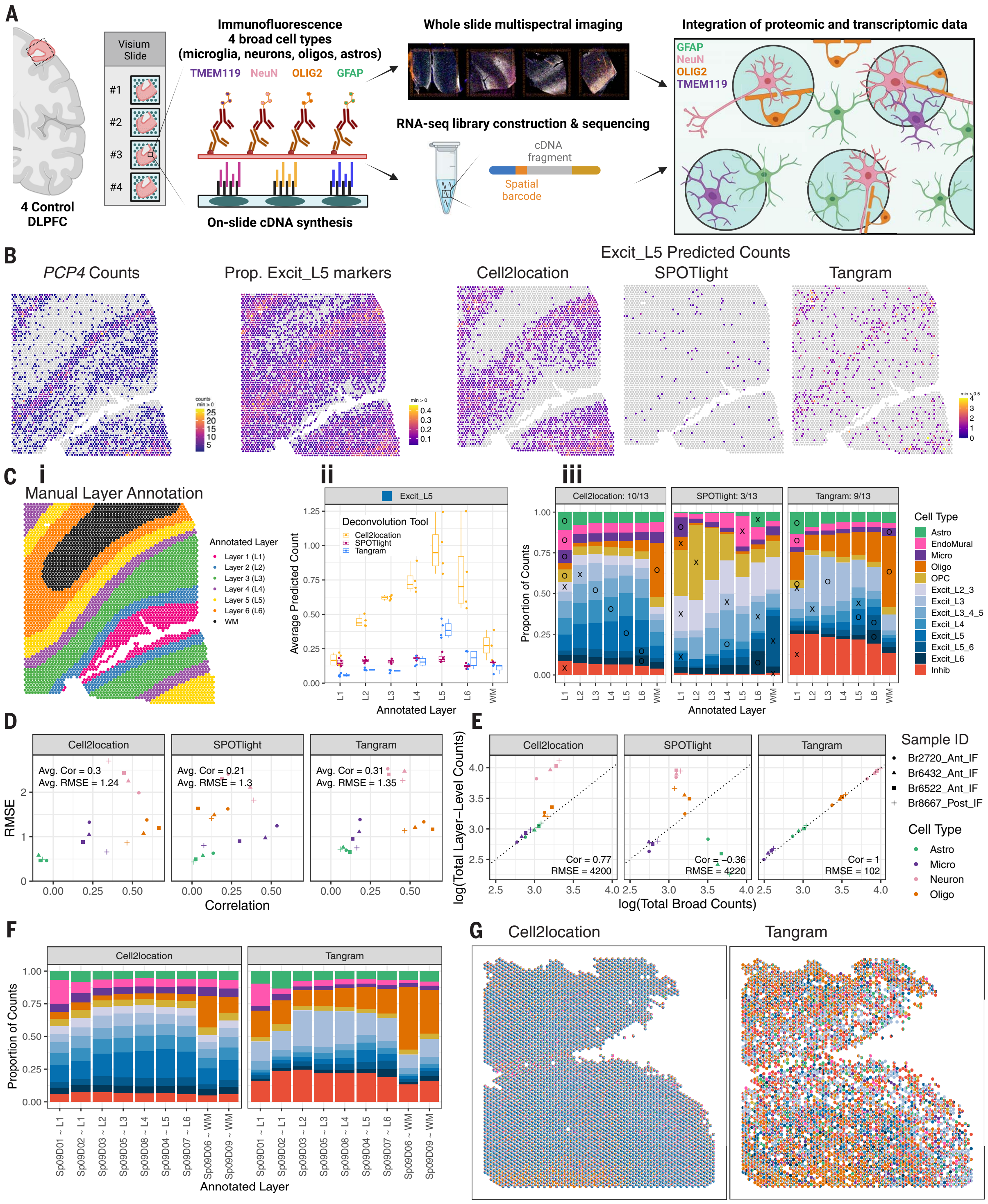

Fig. 4. Integration of snRNA-seq and Visium data to benchmark spot deconvolution algorithms and define cellular composition across SpDs. (**A**) Schematic of the Visium-SPG protocol. (**B**) For Br6522_Ant_IF, counts for L5 marker gene *PCP4* are compared with the proportion of Excit_L5 marker genes with nonzero expression as well as the counts of Excit_L5 cells as predicted by the three evaluated deconvolution algorithms. (**C**) (i) Example of manually annotated layer assignments for Br6522_Ant_IF, which are used to benchmark predicted cell type composition across layers. (ii) Using Excit_L5 as an example, predicted Excit_L5 counts for each method are averaged across all spots within each annotated layer for each tissue section. (iii) These data are summarized across layers and tissue sections for the 13 cell types by use of a bar plot. An "X" or "O" indicates the layer with maximal proportion; an "O" indicates a "correct" match for the given cell type, and an "X" indicates otherwise. For example, *Tangram* correctly predicts the maximal proportion of Excit_L5 cells in L5 annotated spots, leading to the placement of an "O" for Excit_L5. The "O"s are tallied for each method to generate a summary score in each facet's title (for example, 9 of 13 cell types were correctly predicted to the expected layer by using *Tangram*). (**D**) Predicted counts for a given method, section, and layer-level cell type are collapsed and compared against the corresponding CART predictions by computing the Pearson correlation and root mean squared error

(RMSE), forming a single point in the scatterplot (SM, "Evaluating performance of spot-deconvolution methods"). Each of these values is then averaged to generate a single correlation and RMSE value for each method, indicated at top left inside each plot facet. (**E**) Section-wide counts for each cell type are compared between broad and layer-level resolutions, collapsed onto the cell type resolution used by the CART, where values theoretically should precisely match. (**F**) The predicted proportion of cells in each Sp_9D, deconvoluted by *Cell2location* and *Tangram*, is averaged across all Visium samples (n = 30). (**G**) Cell composition of each Visium spot for Br8667_mid, deconvoluted by *Cell2location* and *Tangram*, revealing differences in cell composition prediction.

(LR) interactions associated with neuropsychiatric disorders. We focused on genetic risk for SCZ because receptors occur more frequently in SCZ risk genes than would be expected of a brain-expressed gene list of this size (P < 0.0001) (fig. S42A). First, we identified interacting cell types using CCC analysis (*18*), which uses a data-driven approach to predict cross-talk between sender and receiver cells on the basis of known LR interactions (Fig. 5A and table S3). In parallel, using the OpenTargets and Omnipath databases (*32*, *33*), we identified 834 LR pairs (table S4) associated with genetic risk for SCZ. Of these, 90 interactions overlapped with those identified in CCC analysis where at least one of the interactors was associated with SCZ risk (table S5).

We chose to prioritize 18 inter- and intracellular interactions in which both counterparts showed disease association, including nine interactions involving the protein tyrosine kinase *FYN* (Fig. 5A and fig. S42). A consensus LR pair was identified between these complementary data-driven and clinical risk–driven approaches: the membrane-bound ligand ephrin A5 (*EFNA5*) and its receptor ephrin type-A receptor 5 (*EPHA5*). As part of this signaling cascade, we also evaluated the intracellular interaction between *EFNA5* and *FYN*, which was one of the 18 SCZ-associated LR pairs (Fig. 5A).

The Ephrin-Eph signaling system is critical for neuronal wiring during brain development and neural plasticity and synaptic homeostasis in adulthood (*34*). To better understand the role of this SCZ-associated signaling pathway in the adult DLPFC, we next characterized the cell types mediating this interaction using our snRNA-seq data. We identified enrichment of *EFNA5*, *EPHA5*, and *FYN* in excitatory neuron populations (Fig. 5C), which are the dominant sender and receiver cells for this LR interaction (Fig. 5B). Particularly, Excit_L5/6 neurons most specifically expressed the ligand *EFNA5* [specificity measure (SPM) = 0.6847] and its intracellular partner *FYN* (SPM = 0.5345), whereas Excit_L6 neurons most specifically expressed the receptor *EPHA5* (SPM = 0.6508) (fig. S42B). Furthermore, Excit_L5 and Excit_L6 neurons showed the highest coexpression of *FYN* and *EFNA5*, coexpressing in 87.25% of this population (Fig. 5D).

Because *EFNA5-EPHA5* is a contact-dependent interaction (*34*), we used the Visium data to spatially map sites of likely *EFNA5* and *EPHA5* cross-talk. Across data-driven SpDs, the highest proportion of spots coexpressing *EFNA5* and *EPHA5* localized to Sp_9D_7 ~ L6 [median (interquartile range) = 0.0196 (0.0137), $P = 4.0 \times {}^{-09}$] (Fig. 5, E and F) compared with other Sp_9Ds [Sp_9D_1 = 0 (0), Sp_9D_2 = 0 (0), Sp_9D_3 = 0.0052 (0.0078), Sp_9D_4 = 0.014 (0.0142), Sp_9D_5 = 0.0091 (0.0102), Sp_9D_6 = 0 (0.0016), Sp_9D_8 = 0.0077 (0.0123), and Sp_9D_8 = 0.0016 (0.0104)]. Consistent with snRNA-seq specificity analysis (fig. S42, B and C), spots coexpressing *EFNA5* and *EPHA5* showed a higher predicted proportion of Excit_L5/6 neurons and Excit_L6 neurons compared with spots lacking coexpression (Fig. 5H and fig. S43). Although Excit_L5 is the dominant *cell2location* predicted cell type among all spots (figs. S41 and S43B), it is even higher among these coexpression spots (median predicted proportion = 0.211) than among other spots (fig. S43). Spatial network analyses further supported that colocalization of *EFNA5* and *EPHA5* occurs frequently in spots containing Excit_L6 neurons, with strongest colocalization relationships between Excit_L6/Excit_L5 neurons, Excit_L6/Excit_L4 neurons, and Excit_L6/oligodendrocytes (Fig. 5I and fig. S42D). Spatial mapping of *EFNA5* and *FYN* interactions also showed significant coexpression of these genes in Sp_9D_7~L6 (P = 0.0046) (fig. S42, F and G), with frequent colocalization between Excit_L5/L6 and Excit_4 neurons (fig. S42, H and I). We demonstrate the utility of these integrated single-cell and spatial transcriptomic data for identifying and mapping disease-associated interactions in spatially localized cell types across the human DLPFC.

Spatial registration of cell populations across neuropsychiatric disorders

To leverage the large amount of snRNA-seq data collected across the PEC (*35*, *36*), we spatially registered eight DLPFC snRNA-seq datasets generated in the context of several brain disorders (ASD, SCZ, bipolar disorder, and Williams Syndrome) to both the histological layers and unsupervised SpDs annotated in Visium data (Fig. 6A and fig. S44). Across the consortium, in neurotypical controls, we found that excitatory neuron subtypes with a laminar annotation spatially register to the relevant histological layers and converge on the same unsupervised SpDs. As expected, most inhibitory populations registered to multiple histological layers and unsupervised SpDs, with the exception of Pvalb and vascular lepotomeningeal cell (VLMC) subtypes, which mapped to Sp_9D_8~L4 and Sp_9D_1~L1, respectively. Last, glial populations also showed expected spatial registration, with astrocytes strongly mapping to L1-associated SpDs; oligodendrocytes and OPCs strongly mapping to the WM; and endothelial, pericyte (PC), and smooth muscle cells (SMCs) mapping to the newly characterized vascular domain Sp_9D_1.

Next, we spatially registered snRNA-seq data from 30,147 nuclei derived from the human prefrontal cortex (Brodmann areas unspecified) from control donors in a study of ASD (Fig. 6B) (*20*). As expected, glial populations and laminar excitatory cell types mapped to the relevant SpDs (L2/3 neurons mapped to Sp_9D_3 ~ L2 and Sp_9D_5 ~ L3). We were also able to provide laminar assignments to some cell populations, such as mapping neurogranin (NRGN) neuronal subtypes to Sp_9D_5 ~ L3 and Sp_9D_8 ~ L4. For each cell type, we next used clinical gene set enrichment analyses to assess the SpD enrichment of cell type–specific DEGs between individuals with ASD compared with neurotypical controls (Fig. 6C). Across many cell types, we observed multiple Sp_9Ds enriched for ASD DEGs. Sp_9D_3~L2 showed significant enrichment of genes differentially expressed in L2/3 nuclei between individuals with ASD and neurotypical controls ($P = 2.60 \times 10^{-11}$), highlighting that these L2/3 DEGs are core Sp_9D_3 ~ L2 marker genes. We also identified spatial enrichments for DEGs expressed in inhibitory neuron and NRGN populations, including Sp_9D_4 ~ L5 for synaptic vesicle glycoprotein 2C (SV2C) inhibitory neurons and Sp_9D_7~L6 for Neu_NRGN_I neurons. Last, to demonstrate how this large-scale dataset can be used to provide spatial information about genes associated with neuropsychiatric disease, we performed gene set enrichment analysis of bulk RNA-seq DEGs identified in a companion PEC study of PTSD and MDD (PEC study 6) (*23*). For both DLPFC and the ventral medial prefrontal cortex (mPFC), we demonstrated that vasculature domain Sp_9D_1~L1 and L1-associated domain Sp_9D_2~L1 are enriched in DEGs associated with both PTSD and MDD. This is consistent with previous studies that implicated neuroimmune signaling in PTSD (*37*) and current PEC single-cell analyses that implicate glial and vascular cells in both MDD and PTSD (PEC study 6) (*23*). Together, these spatial registration and clinical gene set enrichment analyses add anatomical context to cell type identities and provide valuable biological insights into molecular changes associated with brain disorders, including ASD, MDD, and PTSD.

Discussion

We have generated a large-scale, transcriptome-wide, data-driven molecular map across the

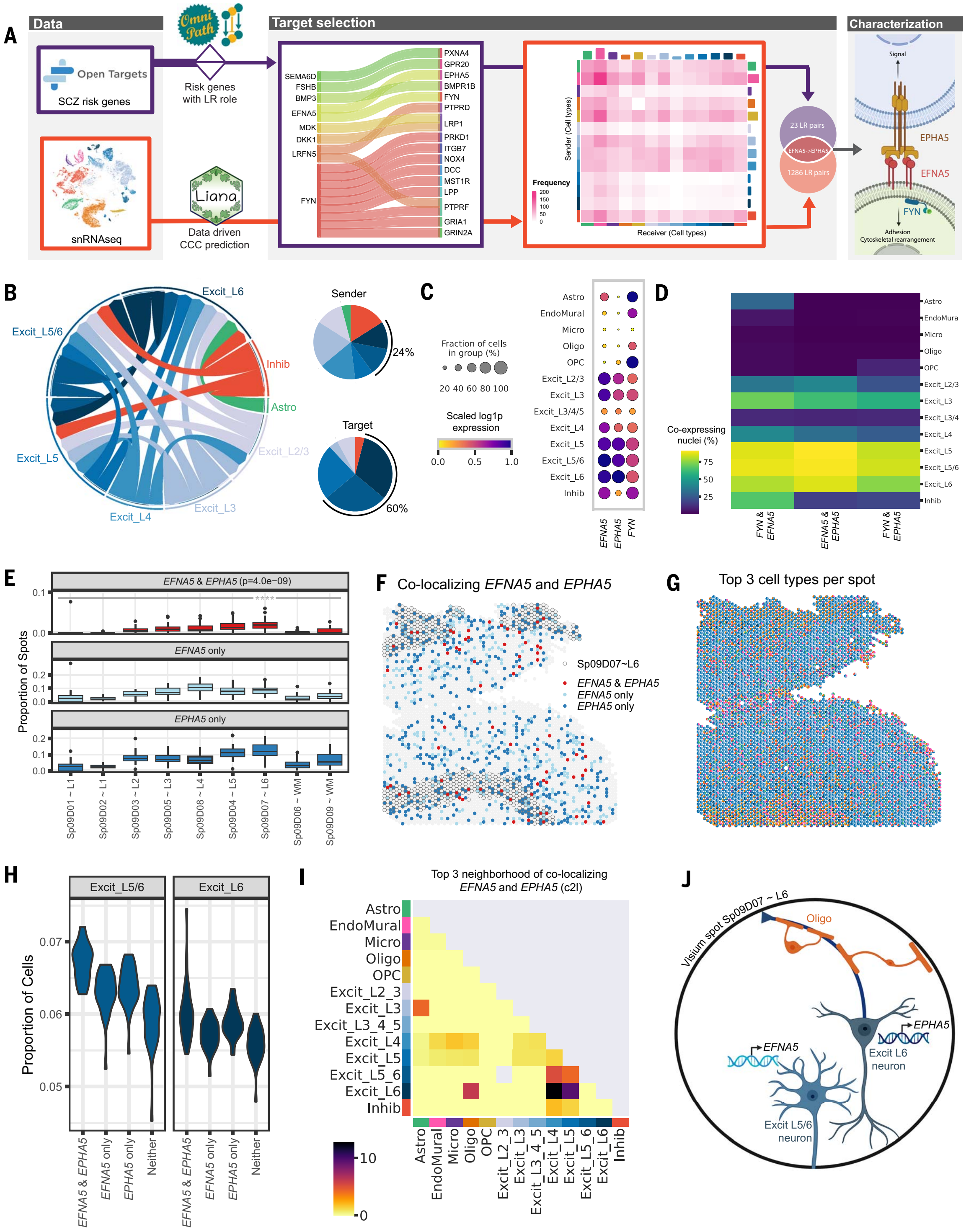

Fig. 5. SCZ-associated LR interactions identified with integrative analysis of snRNA-seq and Visium data. (**A**) The LR interaction between membrane-bound ligand ephrin A5 (*EFNA5*) and ephrin type-A receptor 5 (*EPHA5*) is a consensus target identified in both data-driven (table S3) and clinical risk–driven LR (table S4) analyses. This interaction also requires an intracellular interaction between *EFNA5* and protein tyrosine kinase (*FYN*), which was also identified among clinical risk targets. (**B**) CCC analysis predicts the sender-receiver cross-talk pattern of *EFNA5-EPHA5* between layer-level cell types visualized in a circular plot. Excit_L5/6 and Excit_L6 neurons account for 24% of the cross-talk as senders and 60% as targets compared with other cell types shown in the pie charts. (**C** and **D**) Downstream analysis of snRNA-seq data characterizes *FYN-EFNA5-EPHA5* signaling pathway, showing that these genes are (C) highly enriched and (D) coexpressed in excitatory neuron populations. (**E**) Across all 30 tissue sections, *EFNA5* and *EPHA5* are coexpressed in a statistically higher proportion of spots in Sp$_9$D$_7$ [median (interquartile range) = 0.0196 (0.0137), $P = 4.0 \times 10^{-09}$] as compared with other Sp$_9$Ds [Sp$_9$D$_1$ = 0 (0), Sp$_9$D$_2$ = 0 (0), Sp$_9$D$_3$ = 0.0052 (0.0078), Sp$_9$D$_4$ = 0.0140 (0.0142), Sp$_9$D$_5$ = 0.0091 (0.0102), Sp$_9$D$_6$ = 0 (0.0016), Sp$_9$D$_8$ = 0.0077 (0.0123), and Sp$_9$D$_8$ = 0.0016 (0.0104)]. (**F**) Spotplot of *EFNA5* and *EPHA5* coexpression in Br8667_mid. (**G**) Spotplot with spot-level pie charts for Br8667_mid showing the top three dominant cell types in

each Visium spot predicted by *Cell2location* (*c2l*). (**H**) Visium spots coexpressing *EFNA5* and *EPHA5* have higher proportions of predicted Excit_L5/6 neurons ($P = 1.8 \times 10^{-12}$) and Excit_L6 (P=3.9 × 10^{-4}) compared with those of noncoexpressing spots, which is consistent with snRNA-seq specificity analyses (fig. S42). Few other cell types show this relationship (fig. S43). Complementary analyses of *EFNA5* and *FYN* coexpression are shown in fig. S42. (**I**) Spatial network analysis of all 30 tissue sections, using top three dominant *c2l* cell types in each spot [exemplified in (G) with Br8667_mid], confirms that *EFNA5* and *EPHA5* coexpression occurs frequently in spots containing Excit_L6 neurons. Complementary analyses by using the top six dominant *c2l* cell types as well as *Tangram* predictions are reported in fig. S42. (**J**) Schematic of a Visium spot depicting *EFNA5-EPHA5* interactions between Excit_L5/6 neurons and Excit_L6. The high colocalization score in the spatial network analysis in (I) suggests that oligodendrocytes also likely coexist with Excit_L6 neurons.

anterior-posterior axis of the adult human DLPFC from 10 neurotypical control donors. This highly integrated single-cell and spatial gene expression reference dataset enabled identification of unsupervised SpDs, which were characterized in terms of both cellular composition and domain-enriched genes, at different resolutions across the DLPFC. We have provided a landmark molecular neuroanatomical atlas that complements our understanding of classic cortical cytoarchitecture through identification and characterization of discrete molecularly defined layers and sublayers. In particular, we annotated a vasculature-rich meninges layer and several molecularly distinct subdomains in histological L1, L4, L5, and L6. An advantage of Visium over snRNA-seq approaches is the ability to capture transcripts in the cell cytoplasm and neuropil, which we speculate may influence identification of higher-resolution SpDs, particularly for demarcating laminar transitions and at the gray matter–WM junction (*38*–*40*).

In this study, we have provided a roadmap for the implementation and biological validation of unsupervised spatial clustering approaches in human brain tissue. Whereas manual annotation of SpDs is feasible for a limited number of samples in brain regions where neuroanatomical boundaries are well characterized (*12*, *22*), the application of data-driven clustering methods is critical for future studies that aim to analyze spatial gene expression changes across diagnostic cohort groups to identify changes in spatially resolved cell types. Furthermore, unsupervised approaches will be essential for spatial profiling in brain regions that lack clear molecular or histological boundaries because they allow for identification of unknown or unexpected SpDs as well as SpDs that may be technically difficult to manually annotate (for example, the meninges). Although in this study we evaluated several of the spatial clustering algorithms, including *SpaGCN* and *BayesSpace* (*13*, *15*), there are more tools coming online for both spatially variable gene detection, including *nnSVG* (*41*), and also SpD identification, including *GraphST* and *PRECAST* (*16*, *17*). Large-scale, integrated datasets, including the present study, continue to offer developers of computational tools opportunities to develop methods scalable to atlas-level data while also extracting meaningful biological information.

Visium offers transcriptome-wide information at spatial resolution; however, a limitation of the platform is that spots often contain multiple cells and cell types. We believe that this might be overcome by using spot-level deconvolution tools, as we describe here. We rigorously benchmarked the utility of these tools against Visium-SPG data in the DLPFC, where we manually assigned spots to the histological layers while also immunolabeling four broad cell populations in the same tissue sections. From these data, we predicted the proportion of cell types in each spot, allowing us to achieve cellular resolution for our spatiomolecular map. Although spatial registration correlation approaches can be informative for broadly mapping cell types to SpDs, spot deconvolution approaches provide higher-resolution mapping across the cortical layers. This is especially evident for glial cell populations, which show the strongest spatial registration correlations to L1 and WM but are indeed localized to all other SpDs when performing spot deconvolution. This is also true for endothelial cells, which are strongly associated with vasculature-enriched Sp_9D_1~L1 but are similarly distributed across the cortex when using spot deconvolution approaches. As spot deconvolution tools continue to improve with the emergence of more large-scale single-cell and spatial transcriptomic datasets, we expect that algorithms will be able to map finer-resolution and rarer cell types.

Although other imaging-based, spatially resolved transcriptomics platforms such as Xenium and multiplexed error robust fluorescence in situ hybridization (MERFISH) (*42*, *43*) directly measure transcripts in individual cells, only a limited number of genes can currently be probed. By contrast, the discovery-based approach afforded by Visium, as well as its scalability to a large number of samples, allowed for robust identification of previously unrecognized spatial marker genes across many donors. These Visium-identified genes can be followed up at single-cell resolution in smaller cohorts by using probe-based approaches, such as MERFISH, which was recently applied to the middle and superior temporal gyri in the human brain (*44*). As spatial transcriptomics technologies continue to evolve, it will be important to functionally validate these SpDs and consider the biological role of these molecularly defined compartments. Previous spatial transcriptomic studies in the mouse brain identified distinct astrocyte layers that diverge from classic excitatory neuron layers (*45*), suggesting that the cortex likely has a more complex laminar architecture than previously appreciated. Future studies should evaluate the conservation of laminar SpDs between rodent and human brain and explore their functional and clinical relevance.

In terms of clinical relevance, alterations in neural activity patterns within the DLPFC have been noted in several neurodevelopmental and neuropsychiatric disorders (*46*–*49*), and it is hypothesized that changes in molecular signaling cascades may contribute to these alterations in activity. To gain insight into molecular dysfunction in DLPFC in the context of disease, we used our integrated molecular atlas to spatially map cell type–specific LR interactions that are associated with genetic risk for SCZ. For example, we highlight the interaction between *EFNA5* and *EPHA5* in excitatory L5/6 and L6 neuron subtypes in deep cortical layers, which is consistent with results from the most recently released SCZ genome-wide association study (GWAS) that identified enrichment of SCZ risk genes in glutamatergic neurons (*50*). Not only is *EFNA5* the locus of a GWAS-identified common SCZ risk variant, it is also differentially expressed between individuals with SCZ and neurotypical controls in specific cell types (*21*). Spatially mapping disease-relevant LR pairs, which are often highly specific and druggable targets, can provide valuable insights into pathophysiology and can help prioritize spatially restricted targets for therapeutic development. In combination with our interactive web resources, this highly integrated single-cell and spatial transcriptomic data from neurotypical control DLPFC can be used to accelerate research across a variety of brain disorders by allowing researchers to search for relevant genes of interest, spatially register clinical gene sets, and explore disease-associated cell types for complementary assays, such as in vitro disease models.

Last, spatial registration of eight DLPFC snRNA-seq datasets collected across the PEC in the context of different neuropsychiatric disorders (*35*) revealed a convergence of excitatory, inhibitory, and non-neuronal cell types in relevant SpDs. We observed increased confidence of inhibitory neuron mapping in our current expanded study compared with (*12*), likely because of the larger donor/sample number and data-driven clustering approach, which allowed for identification of finer-resolution SpDs. Furthermore, using ASD as an example (*20*), we demonstrated the utility of our data-driven molecular atlas for localizing cell type–specific DEGs to

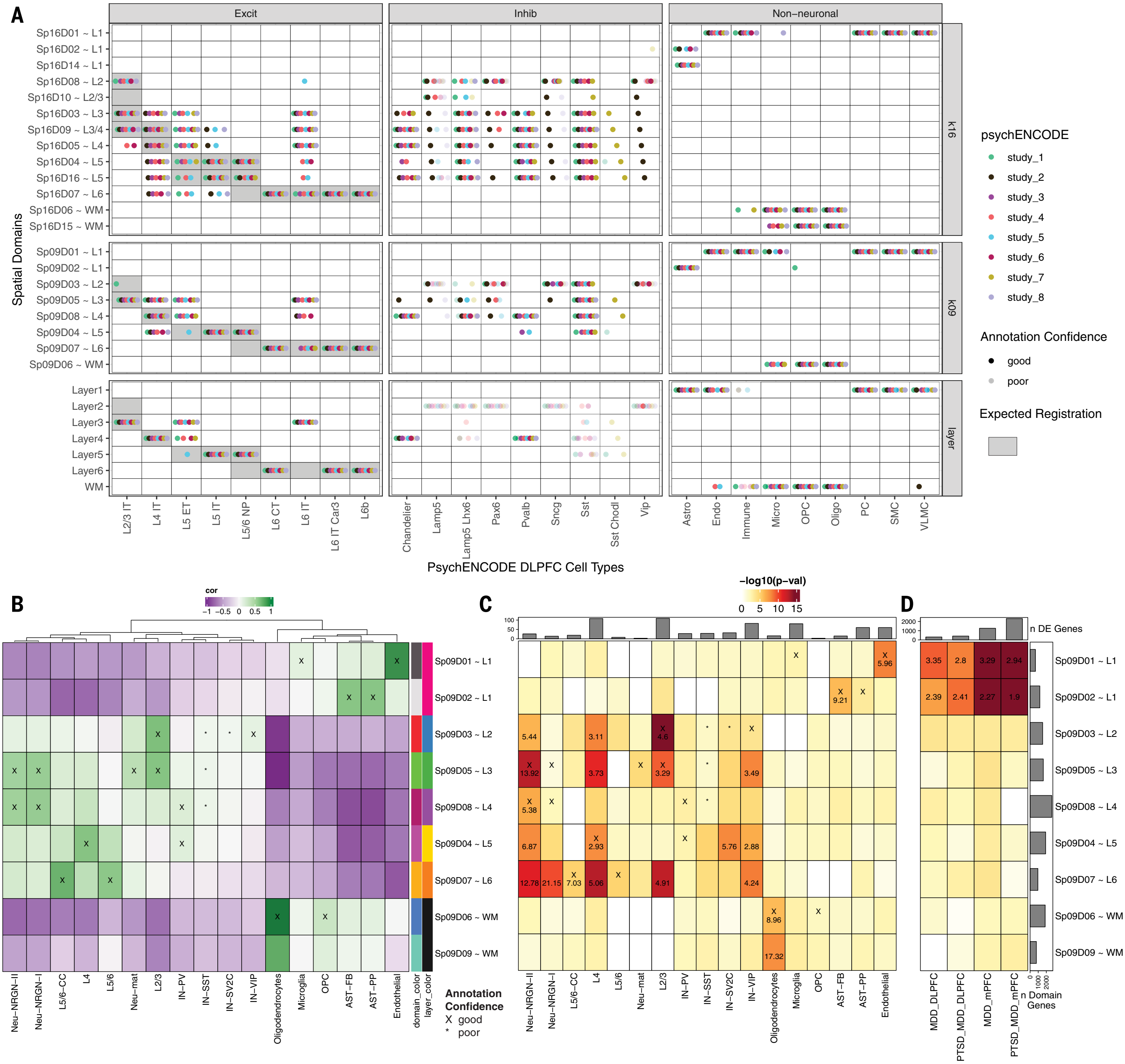

Fig. 6. Spatial enrichment of cell types and genes associated with neurodevelopmental and neuropsychiatric disorders. (**A**) Dot plot summarizing spatial registration results for eight PEC snRNA-seq datasets from human DLPFC. snRNA-seq data were uniformly processed through the same pipeline and annotated with common nomenclature based on work from the Allen Brain Institute (*35*, *69*). Registration was performed for control donors only (the full dataset is available in fig. S44) across manually annotated histological layers from (*12*) as well as unsupervised *BayesSpace* clusters at *k* = 9 and 16 (Sp_9Ds and $Sp_{16}Ds$, respectively). Each dot indicates the histological layer(s) or SpD(s) where a dataset's cell type was annotated during spatial registration. Solid dots indicate good confidence in the spatial annotation, and translucent dots indicate poor confidence in the annotation. IT, intratelencephalon-projecting; ET, extratelencephalon-projecting; CT, corticothalamic-projecting; NP, near-projecting; VLMC, vascular lepotomeningeal cell; OPC, oligodendrocyte precursor cell; PC, pericyte; SMC, smooth muscle cell. (**B**) Spatial registration of cell type populations from control samples from (*20*) against unsupervised *BayesSpace* clusters at *k* = 9 (Sp_9Ds). Higher-confidence annotations (cor > 0.25, merge ratio = 0.1) (SM, "Spatial registration of PsychENCODE and other external snRNA-seq datasets") are indicated with an "X." (**C**) Enrichment analysis by using Fisher's exact test for Sp_9D-enriched statistics versus DEGs (FDR < 0.05) in ASD for each cell type population. The values are the odds ratios (ORs) for the enrichment in significant (FDR < 0.001) blocks of the heatmap, and the color scale indicates −log10(*P* value) for the enrichment test. The top bar plot shows the number of DEGs for each cell type. (**D**) Enrichment analysis by using Fisher's exact test for Sp_9D-enriched statistics versus DEGs (FDR < 0.05) in PTSD and/or MDD in bulk RNA-seq of DLPFC and mPFC (*23*). Top bar plot indicates the number of DEGs for each DE test. Left bar plot indicates the number of significantly enriched genes for each Sp_9D in both enrichment analyses.

specific SpDs. For example, ASD DEGs in vasoactive intestinal peptide (VIP) inhibitory neurons were enriched in L3-, L5-, and L6-associated SpDs, whereas those in SV2C inhibitory neurons were enriched only in the L5-associated domain. Together, this analysis provides anatomical context for cell type–specific gene expression changes and molecular mechanisms associated with neurodevelopmental disorders and psychiatric illness.

We have provided a large-scale, highly integrated single-cell and spatial transcriptomics resource for understanding the molecular neuroanatomy of the human DLPFC. We share web-based tools for the scientific community to interact with these datasets for further interrogation of molecular pathways associated with brain disorders.

Materials and methods summary

Detailed materials and methods can be found in the supplementary materials. Three tissue blocks from the anterior, middle, and posterior positions along the rostral-caudal axis of human DLPFC were microdissected from the post-mortem brains of 10 donors for a total of 30 tissue blocks. The 10x Genomics Visium Spatial Gene Expression protocol was performed on all blocks (n = 30). The 10x Genomics Visium SPG and 3′ Single Cell Gene Expression protocols were performed on a subset of blocks (n = 4 and 19, respectively). Visium and Visium SPG data were processed with 10x Genomics SpaceRanger (51). Dimensionality reduction was performed by using *scater* (52), and batch correction was performed with *Harmony* (53). Unsupervised clustering was performed on the Visium data with *BayesSpace* (13) defining data-driven SpDs. An optimal number of SpDs was determined with *fasthplus* (54). DEGs between SpDs were found with ANOVA, enrichment, and pairwise models with tools from *spatialLIBD* (55), powered by *limma* (56). snRNA-seq data were processed with 10x Genomics CellRanger (57). Reduced dimensions were calculated with GLM-PCA (58), and batch correction was performed with *Harmony* (53). Graph-based and hierarchical clustering described in (59) identified cell type populations, which were annotated by using established marker genes (59, 60). Spatial registration was applied to snRNA-seq and SpDs with tools from *spatialLIBD* (55). Images from Visium and Visium SPG were processed with *VistoSeg* (61). Nuclei were segmented with *Cellpose* (62). A decision-tree cell type classifier was built with *scikit-learn* (63) on the basis of a training set classified by an expert. Cell segmentation and classification from Visium-SPG was used to benchmark spot deconvolution algorithms *Tangram*, *Cell2Location*, and *SPOTlight* (14, 30, 31). Spot deconvolution on the 30 Visium samples was performed with both *Tangram* and *Cell2Location*. CCC was performed with *LIANA* (18). The SCZ risk gene list was obtained from *OpenTargets* (32). Spatial registration was performed on the uniformly processed PsychENCODE snRNA-seq datasets (35). Enrichment statistics were calculated with *spatialLIBD* for the DEGs in an ASD snRNA-seq dataset (20) and bulk RNA-seq PTSD and MDD dataset (23).

REFERENCES AND NOTES

1. E. Madissoon *et al*., A spatially resolved atlas of the human lung characterizes a gland-associated immune niche. *Nat. Genet.* **55**, 66–77 (2023). doi: 10.1038/s41588-022-01243-4; pmid: 36543915
2. C. Ortiz *et al*., Molecular atlas of the adult mouse brain. *Sci. Adv.* **6**, eabb3446 (2020). doi: 10.1126/sciadv.abb3446; pmid: 32637622
3. M. Asp *et al*., A spatiotemporal organ-wide gene expression and cell atlas of the developing human heart. *Cell* **179**, 1647–1660.e19 (2019). doi: 10.1016/j.cell.2019.11.025; pmid: 31835037
4. F. Hildebrandt *et al*., Spatial Transcriptomics to define transcriptional patterns of zonation and structural components in the mouse liver. *Nat. Commun.* **12**, 7046 (2021). doi: 10.1038/s41467-021-27354-w; pmid: 34857782
5. D. J. Di Bella *et al*., Molecular logic of cellular diversification in the mouse cerebral cortex. *Nature* **595**, 554–559 (2021). doi: 10.1038/s41586-021-03670-5; pmid: 34163074
6. D. W. Volk, D. A. Lewis, Prefrontal cortical circuits in schizophrenia. *Curr. Top. Behav. Neurosci.* **4**, 485–508 (2010). doi: 10.1007/7854_2010_44; pmid: 21312410
7. D. R. Weinberger, Schizophrenia, the prefrontal cortex, and a mechanism of genetic susceptibility. *Eur. Psychiatry* **17** (Suppl 4), 355s–362s (2002). doi: 10.1016/S0924-9338(03)00080-4; pmid: 23573605
8. M. Koenigs, J. Grafman, The functional neuroanatomy of depression: Distinct roles for ventromedial and dorsolateral prefrontal cortex. *Behav. Brain Res.* **201**, 239–243 (2009). doi: 10.1016/j.bbr.2009.03.004; pmid: 19428640
9. N. J. Gamo, A. F. T. Arnsten, Molecular modulation of prefrontal cortex: Rational development of treatments for psychiatric disorders. *Behav. Neurosci.* **125**, 282–296 (2011). doi: 10.1037/a0023165; pmid: 21480691
10. M. A. Cerullo, C. M. Adler, M. P. Delbello, S. M. Strakowski, The functional neuroanatomy of bipolar disorder. *Int. Rev. Psychiatry* **21**, 314–322 (2009). doi: 10.1080/09540260902962107; pmid: 20374146
11. H. R. Willsey, A. J. Willsey, B. Wang, M. W. State, Genomics, convergent neuroscience and progress in understanding autism spectrum disorder. *Nat. Rev. Neurosci.* **23**, 323–341 (2022). doi: 10.1038/s41583-022-00576-7; pmid: 35440779
12. K. R. Maynard *et al*., Transcriptome-scale spatial gene expression in the human dorsolateral prefrontal cortex. *Nat. Neurosci.* **24**, 425–436 (2021). doi: 10.1038/s41593-020-00787-0; pmid: 33558695
13. E. Zhao *et al*., Spatial transcriptomics at subspot resolution with BayesSpace. *Nat. Biotechnol.* **39**, 1375–1384 (2021). doi: 10.1038/s41587-021-00935-2; pmid: 34083791
14. T. Biancalani *et al*., Deep learning and alignment of spatially resolved single-cell transcriptomes with Tangram. *Nat. Methods* **18**, 1352–1362 (2021). doi: 10.1038/s41592-021-01264-7; pmid: 34711971
15. J. Hu *et al*., SpaGCN: Integrating gene expression, spatial location and histology to identify spatial domains and spatially variable genes by graph convolutional network. *Nat. Methods* **18**, 1342–1351 (2021). doi: 10.1038/s41592-021-01255-8; pmid: 34711970
16. W. Liu *et al*., Probabilistic embedding, clustering, and alignment for integrating spatial transcriptomics data with PRECAST. *Nat. Commun.* **14**, 296 (2023). doi: 10.1038/s41467-023-35947-w; pmid: 36653349
17. Y. Long *et al*., Spatially informed clustering, integration, and deconvolution of spatial transcriptomics with GraphST. *Nat. Commun.* **14**, 1155 (2023). doi: 10.1038/s41467-023-36796-3; pmid: 36859400
18. D. Dimitrov *et al*., Comparison of methods and resources for cell-cell communication inference from single-cell RNA-Seq data. *Nat. Commun.* **13**, 3224 (2022). doi: 10.1038/s41467-022-30755-0; pmid: 35680885
19. C. Nagy *et al*., Single-nucleus transcriptomics of the prefrontal cortex in major depressive disorder implicates oligodendrocyte precursor cells and excitatory neurons. *Nat. Neurosci.* **23**, 771–781 (2020). doi: 10.1038/s41593-020-0621-y; pmid: 32341540
20. D. Velmeshev *et al*., Single-cell genomics identifies cell type–specific molecular changes in autism. *Science* **364**, 685–689 (2019). doi: 10.1126/science.aav8130; pmid: 31097668
21. W. B. Ruzicka *et al*., Single-cell multi-cohort dissection of the schizophrenia transcriptome. *Science* **384**, eadg5136 (2022).
22. M. Y. Batiuk *et al*., Upper cortical layer-driven network impairment in schizophrenia. *Sci. Adv.* **8**, eabn8367 (2022). doi: 10.1126/sciadv.abn8367; pmid: 36223459
23. N. P. Daskalakis *et al*., Systems Biology Dissection of PTSD and MDD across brain regions, cell-types and blood. *Science* **384**, eadh3707 (2024).
24. 10x Genomics, Visium Spatial Gene Expression; https://www.10xgenomics.com/products/spatial-gene-expression.
25. G. Csardi, T. Nepusz, The Igraph software package for complex network research. *InterJournal* **2006**, 1695 (2006).
26. A. T. L. Lun, D. J. McCarthy, J. C. Marioni, A step-by-step workflow for low-level analysis of single-cell RNA-seq data with Bioconductor. *F1000Res.* **5**, 2122 (2016). doi: 10.12688/f1000research.9501.2; pmid: 27909575
27. R. D. Hodge *et al*., Conserved cell types with divergent features in human versus mouse cortex. *Nature* **573**, 61–68 (2019). doi: 10.1038/s41586-019-1506-7; pmid: 31435019
28. Y. Hao *et al*., Integrated analysis of multimodal single-cell data. *Cell* **184**, 3573–3587.e29 (2021). doi: 10.1016/j.cell.2021.04.048; pmid: 34062119
29. T. E. Bakken *et al*., Comparative cellular analysis of motor cortex in human, marmoset and mouse. *Nature* **598**, 111–119 (2021). doi: 10.1038/s41586-021-03465-8; pmid: 34616062
30. M. Elosua-Bayes, P. Nieto, E. Mereu, I. Gut, H. Heyn, SPOTlight: Seeded NMF regression to deconvolute spatial transcriptomics spots with single-cell transcriptomes. *Nucleic Acids Res.* **49**, e50 (2021). doi: 10.1093/nar/gkab043; pmid: 33544846
31. V. Kleshchevnikov *et al*., Cell2location maps fine-grained cell types in spatial transcriptomics. *Nat. Biotechnol.* **40**, 661–671 (2022). doi: 10.1038/s41587-021-01139-4; pmid: 35027729
32. D. Ochoa *et al*., The next-generation Open Targets Platform: Reimagined, redesigned, rebuilt. *Nucleic Acids Res.* **51** (D1), D1353–D1359 (2023). doi: 10.1093/nar/gkac1046; pmid: 36399499
33. D. Türei, T. Korcsmáros, J. Saez-Rodriguez, OmniPath: Guidelines and gateway for literature-curated signaling pathway resources. *Nat. Methods* **13**, 966–967 (2016). doi: 10.1038/nmeth.4077; pmid: 27898060
34. A. Kania, R. Klein, Mechanisms of ephrin-Eph signalling in development, physiology and disease. *Nat. Rev. Mol. Cell Biol.* **17**, 240–256 (2016). doi: 10.1038/nrm.2015.16; pmid: 26790531
35. PsychENCODE Consortium, PsychENCODE Consortium (PEC) Capstone II Cross-study Harmonized Data. *Synapse* (2023); https://doi.org/10.7303/syn51111084.1.
36. P. S. Emani *et al*., Single-cell genomics and regulatory networks for 388 human brains. *Science* **384**, eadi5199 (2024).
37. A. E. Jaffe *et al*., Decoding Shared Versus Divergent Transcriptomic Signatures Across Cortico-Amygdala Circuitry in PTSD and Depressive Disorders. *Am. J. Psychiatry* **179**, 673–686 (2022). doi: 10.1176/appi.ajp.21020162; pmid: 35791611
38. S. Fertuzinhos *et al*., Laminar and temporal expression dynamics of coding and noncoding RNAs in the mouse neocortex. *Cell Rep.* **6**, 938–950 (2014). doi: 10.1016/j.celrep.2014.01.036; pmid: 24561256
39. A. Paul *et al*., Transcriptional architecture of synaptic communication delineates GABAergic neuron identity. *Cell* **171**, 522–539.e20 (2017). doi: 10.1016/j.cell.2017.08.032; pmid: 28942923
40. J. D. Perez *et al*., Subcellular sequencing of single neurons reveals the dendritic transcriptome of GABAergic interneurons. *eLife* **10**, e63092 (2021). doi: 10.7554/eLife.63092; pmid: 33404500
41. L. M. Weber, A. Saha, A. Datta, K. D. Hansen, S. C. Hicks, nnSVG for the scalable identification of spatially variable genes using nearest-neighbor Gaussian processes. *Nat. Commun.* **14**, 4059 (2023). doi: 10.1038/s41467-023-39748-z; pmid: 37429865
42. A. Janesick *et al*., 10x Development Teams, S. Taylor, High resolution mapping of the breast cancer tumor microenvironment using integrated single cell, spatial and in situ analysis of FFPE tissue. *Nat. Commun.* **14**, 8353 (2022).
43. K. H. Chen, A. N. Boettiger, J. R. Moffitt, S. Wang, X. Zhuang, RNA imaging. Spatially resolved, highly multiplexed RNA profiling in single cells. *Science* **348**, aaa6090 (2015). doi: 10.1126/science.aaa6090; pmid: 25858977

44. R. Fang *et al*., Conservation and divergence of cortical cell organization in human and mouse revealed by MERFISH. *Science* **377**, 56–62 (2022). doi: 10.1126/science.abm1741; pmid: 35771910
45. O. A. Bayraktar *et al*., Astrocyte layers in the mammalian cerebral cortex revealed by a single-cell in situ transcriptomic map. *Nat. Neurosci.* **23**, 500–509 (2020). doi: 10.1038/s41593-020-0602-1; pmid: 32203496
46. L. Collado-Torres *et al*., Regional Heterogeneity in Gene Expression, Regulation, and Coherence in the Frontal Cortex and Hippocampus across Development and Schizophrenia. *Neuron* **103**, 203–216.e8 (2019). doi: 10.1016/j.neuron.2019.05.013; pmid: 31174959
47. S. J. Dienel, K. E. Schoonover, D. A. Lewis, Cognitive dysfunction and prefrontal cortical circuit alterations in schizophrenia: Developmental trajectories. *Biol. Psychiatry* **92**, 450–459 (2022). doi: 10.1016/j.biopsych.2022.03.002; pmid: 35568522
48. J. Smucny, S. J. Dienel, D. A. Lewis, C. S. Carter, Mechanisms underlying dorsolateral prefrontal cortex contributions to cognitive dysfunction in schizophrenia. *Neuropsychopharmacology* **47**, 292–308 (2022). doi: 10.1038/s41386-021-01089-0; pmid: 34285373
49. J. A. Miller *et al*., Effects of schizophrenia polygenic risk scores on brain activity and performance during working memory subprocesses in healthy young adults. *Schizophr. Bull.* **44**, 844–853 (2018). doi: 10.1093/schbul/sbx140; pmid: 29040762
50. V. Trubetskoy *et al*, Mapping genomic loci implicates genes and synaptic biology in schizophrenia. *Nature* **604**, 502–508 (2022). doi: 10.1038/s41586-022-04434-5; pmid: 35396580
51. 10x Genomics, spaceranger count, 10x Genomics; https://support.10xgenomics.com/spatial-gene-expression/software/pipelines/latest/using/count.
52. D. J. McCarthy, K. R. Campbell, A. T. L. Lun, Q. F. Wills, Scater: Pre-processing, quality control, normalization and visualization of single-cell RNA-seq data in R. *Bioinformatics* **33**, 1179–1186 (2017). doi: 10.1093/bioinformatics/btw777; pmid: 28088763
53. I. Korsunsky *et al*., Fast, sensitive and accurate integration of single-cell data with Harmony. *Nat. Methods* **16**, 1289–1296 (2019). doi: 10.1038/s41592-019-0619-0; pmid: 31740819
54. N. Dyjack, D. N. Baker, V. Braverman, B. Langmead, S. C. Hicks, A scalable and unbiased discordance metric with H. *Biostatistics* **25**, 188–202 (2023). doi: 10.1093/biostatistics/kxac035; pmid: 36063544
55. B. Pardo *et al*., spatialLIBD: An R/Bioconductor package to visualize spatially-resolved transcriptomics data. *BMC Genomics* **23**, 434 (2022). doi: 10.1186/s12864-022-08601-w; pmid: 35689177
56. M. E. Ritchie *et al*., limma powers differential expression analyses for RNA-sequencing and microarray studies. *Nucleic Acids Res.* **43**, e47 (2015). doi: 10.1093/nar/gkv007; pmid: 25605792
57. 10x Genomics, cellranger count, 10x Genomics; https://support.10xgenomics.com/single-cell-gene-expression/software/pipelines/latest/using/count.
58. F. W. Townes, S. C. Hicks, M. J. Aryee, R. A. Irizarry, Feature selection and dimension reduction for single-cell RNA-Seq based on a multinomial model. *Genome Biol.* **20**, 295 (2019). doi: 10.1186/s13059-019-1861-6; pmid: 31870412
59. M. N. Tran *et al*., Single-nucleus transcriptome analysis reveals cell-type-specific molecular signatures across reward circuitry in the human brain. *Neuron* **109**, 3088–3103.e5 (2021). doi: 10.1016/j.neuron.2021.09.001; pmid: 34582785
60. H. Mathys *et al*., Single-cell transcriptomic analysis of Alzheimer's disease. *Nature* **570**, 332–337 (2019). doi: 10.1038/s41586-019-1195-2; pmid: 31042697
61. M. Tippani *et al*., VistoSeg: Processing utilities for high-resolution images for spatially resolved transcriptomics data. *Biol. Imag.* **3**, e23 (2023).
62. M. Pachitariu, C. Stringer, Cellpose 2.0: How to train your own model. *Nat. Methods* **19**, 1634–1641 (2022). doi: 10.1038/s41592-022-01663-4; pmid: 36344832
63. F. Pedregosa *et al*., Scikit-learn: Machine learning in Python. *J. Mach. Learn. Res.* **12**, 2825–2830 (2011).
64. K. Martinowich, K. Maynard, L. Collado-Torres, National Institute of Mental Health Data Archive. A data-driven single-cell and spatial transcriptomic map of the human prefrontal cortex. NDA (2024); https://doi.org/10.15154/7893-6778.
65. A. Nick-Eagles *et al*., LieberInstitute/spatialDLPFC: v0_prerelease. *Zenodo* (2023); https://doi.org/10.5281/zenodo.7616121.
66. L. Huuki-Myers, L. Collado-Torres, B. Guo, M. N. Nick-Eagles, Tran, LieberInstitute/DLPFC_snRNAseq: v0_prerelease. *Zenodo* (2023); https://doi.org/10.5281/zenodo.7616050.
67. C. Sriworarat *et al*., Performant web-based interactive visualization tool for spatially-resolved transcriptomics experiments. *Biol. Imaging* **3**, e15 (2023). doi: 10.1017/S2633903X2300017X; pmid: 38487694
68. K. Rue-Albrecht, F. Marini, C. Soneson, A. T. L. Lun, iSEE: Interactive SummarizedExperiment Explorer. *F1000Res.* **7**, 741 (2018). doi: 10.12688/f1000research.14966.1; pmid: 30002819
69. S. Ma *et al*., Molecular and cellular evolution of the primate dorsolateral prefrontal cortex. *Science* **377**, eabo7257 (2022). doi: 10.1126/science.abo7257; pmid: 36007006

ACKNOWLEDGMENTS

We thank L. Orzolek and the Johns Hopkins Single Cell and Transcriptomics Core facility for executing all sequencing. We also acknowledge E. Engle and the Johns Hopkins Tumor Microenvironment Lab core facility for assistance with the Vectra Polaris slide scanner. We thank the Joint High Performance Computing Exchange (JHPCE) for providing computing resources for these analyses. While an investigator at LIBD, A. E. Jaffe helped secure funding for this work and contributed to the conceptualization of the spatial registration framework. We thank R. A. Miller for assistance with uploading data to the NIMH Data Archive. We thank W. S. Ulrich for his assistance in deploying the Samui interactive websites. We thank D. R. Weinberger and members of the PsychENCODE Consortium for feedback on the manuscript. We thank A. Deep-Soboslay and her diagnostic team for curation of brain samples. We thank the neuropathology team, especially J. Tooke, for assistance with tissue dissection. We thank the physicians and staff at the brain donation sites and the generosity of donor families for supporting our research efforts. Last, we thank the family of C. Lieber and S. Lieber and the family of M. Maltz and T. Maltz for their generous support of this work. Schematic illustrations were generated by using Biorender. The opinions expressed in this article are the authors' own and do not reflect the view of the National Institute on Aging, the National Institutes of Health, the Department of Health and Human Services, or the United States government. A preprint of this work is available at https://doi.org/10.1101/2023.02.15.528722. **Funding:** Data were generated as part of the PsychENCODE Consortium, supported by U01DA048279, U01MH103339, U01MH103340, U01MH103346, U01MH103365, U01MH103392, U01MH116438, U01MH116441, U01MH116442, U01MH116488, U01MH116489, U01MH116492, U01MH122590, U01MH122591, U01MH122592, U01MH122849, U01MH122678, U01MH122681, U01MH116487, U01MH122509, R01MH094714, R01MH105472, R01MH105898, R01MH109677, R01MH109715, R01MH110905, R01MH110920, R01MH110921, R01MH110926, R01MH110927, R01MH110928, R01MH111721, R01MH117291, R01MH117292, R01MH117293, R21MH102791, R21MH103877, R21MH105853, R21MH105881, R21MH109956, R56MH114899, R56MH114901, R56MH114911, R01MH125516, R01MH126459, R01MH129301, R01MH126393, R01MH121521, R01MH116529, R01MH129817, R01MH117406, and P50MH106934 awarded to authors and collaborators A. Abyzov, N. Ahituv, S. Akbarian, K. Brennand, A. Chess, G. Cooper, G. Crawford, S. Dracheva, P. Farnham, M. Gandal, M. Gerstein, D. Geschwind, F. Goes, J. F. Hallmayer, V. Haroutunian, T. M. Hyde, A. Jaffe, P. Jin, M. Kellis, J.E.K., J. A. Knowles, A. Kriegstein, C. Liu, C. E. Mason, K.M., E. Mukamel, R. Myers, C. Nemeroff, M. Peters, D. Pinto, K. Pollard, K. Ressler, P. Roussos, S. Sanders, N. Sestan, P. Sklar, M. P. Snyder, M. State, J. Stein, P. Sullivan, A. E. Urban, F. Vaccarino, S. Warren, D. Weinberger, S. Weissman, Z. Weng, K. White, A. J. Willsey, H. Won, and P. Zandi. Additional data were provided to the PsychENCODE Consortium, supported by 2015 and 2018 NARSAD Young Investigator grants from the Brain & Behavior Research Foundation awarded to collaborator N. Daskalakis. Funding for these studies was provided by the Lieber Institute for Brain Development (LIBD) and National Institute of Mental Health (NIH) grants U01MH122849 and R01MH123183. A.B. was supported by NIH National Institute of General Medical Sciences (NIGMS) grant R35GM139580. M.G.-P. and M.R. were funded by Aligning Science Across Parkinson's (grants ASAP-000478 and ASAP-000509) through the Michael J. Fox Foundation for Parkinson's Research (MJFF). **Authors contributions:** Conceptualization: L.C.-T., K.R.M., K.M., and S.C.H. Methodology: L.C.-T., L.A.H.-M., K.R.M., K.M., and S.C.H. Software: A.B., A.Se., A.Sp., B.G., C.S., H.R.D., L.C.-T., L.A.H.-M., M.G.-P., M.T., N.J.E., P.R., and S.C.H. Validation: A.Sp., B.G., K.D.M., K.R.M., L.C.-T., L.A.H.-M., M.G.-P., M.T., N.J.E., and S.H.K. Formal analysis: A.Sp., A.B.N., B.G., H.R.D., K.R.M., L.C.-T., L.A.H.-M., M.G.-P., M.T., N.J.E., P.R., and S.C.H. Investigation: A.Sp., K.D.M., S.H.K., K.R.M., S.C.P., and M.N.T. Resources: J.E.K., K.R.M., K.M., L.C.-T., S.C.H., and T.M.H. Data curation: L.A.H.-M., L.C.-T., N.J.E., and A.Sp. Writing – original draft: A.Sp., B.G., K.D.M., K.R.M., K.M., L.C.-T., L.A.H.-M., M.G.-P., M.T., N.J.E., S.C.H., S.C.P., and S.H.K. Writing-review and editing: K.R.M., K.M., L.C.-T., S.C.H., and S.C.P. Visualization: A.Sp., L.A.H.-M., K.R.M., L.C.-T., P.R., M.G.-P., B.G., S.H.K., and N.J.E. Supervision: A.B., L.C.-T., K.R.M., K.M., M.R., S.C.H., and S.C.P. Project administration: L.C.-T., K.R.M., K.M., and S.C.P. Funding acquisition: L.C.-T., K.R.M., K.M., and S.C.H. **Competing Interests:** A.B. was a consultant for Third Rock Ventures and a shareholder in Alphabet. J.E.K. is a consultant on a Data Monitoring Committee for an antipsychotic drug trial for Merck & Co., Inc. **Data and materials availability:** The source data described in this manuscript are available from the National Institute of Mental Health (NIMH) Data Archive (https://nda.nih.gov) (*64*). The source data are also publicly available from the Globus end point "jhpce#spatialDLPFC" and "jhpce#DLPFC_snRNAseq" that are also listed at http://research.libd.org/globus. The raw data provided through Globus include all the FASTQ files and raw image files. Processed data are publicly available from the Bioconductor package *spatialLIBD* version 1.11.7 (*55*) through the fetch_data() function. All source code is publicly available from GitHub and permanently archived at Zenodo: https://github.com/LieberInstitute/spatialDLPFC (*65*) and https://github.com/LieberInstitute/DLPFC_snRNAseq (*66*). We provide several interactive web applications to explore this highly integrated DLPFC dataset as listed at http://research.libd.org/spatialDLPFC/#3interactive-websites. First, we developed two *spatialLIBD* apps (*55*) that allow users to analyze Visium gene expression, cell segmentation, spot deconvolution, and clinical gene set enrichment results at $k = 9$ and $k = 16$. We added a third *spatialLIBD* app for the position DE results and a fourth for the Visium-SPG data. Second, both our Visium H&E ($n = 30$ tissue sections) and Visium-SPG ($n = 4$ tissue sections) data are available through a newly created performant web-based interactive visualization tool called *Samui Browser* (*67*), which allows rapid loading, visualization, and custom annotation of high-resolution images and corresponding gene expression. Last, snRNA-seq data at both fine and laminar resolution as well as pseudo-bulked Visium data ($k = 9$, 16, and 28) are available through *iSEE* apps (*68*) that allows users to visualize expression levels for genes of interest through violin and heatmap plots.

SUPPLEMENTARY MATERIALS

science.org/doi/10.1126/science.adh1938
PsychENCODE Consortium Collaborators
Materials and Methods
Figs. S1 to S44
Tables S1 to S14
References (*70*–*88*)

Submitted 17 February 2023; accepted 6 December 2023
10.1126/science.adh1938

Science
AAAS

A data-driven single-cell and spatial transcriptomic map of the human prefrontal cortex

Louise A. Huuki-Myers, Abby Spangler, Nicholas J. Eagles, Kelsey D. Montgomery, Sang Ho Kwon, Boyi Guo, Melissa Grant-Peters, Heena R. Divecha, Madhavi Tippani, Chaichontat Sriworarat, Annie B. Nguyen, Prashanthi Ravichandran, Matthew N. Tran, Arta Seyedian, PsychENCODE Consortium, Thomas M. Hyde, Joel E. Kleinman, Alexis Battle, Stephanie C. Page, Mina Ryten, Stephanie C. Hicks, Keri Martinowich, Leonardo Collado-Torres, Kristen R. Maynard, Schahram Akbarian, Alexej Abyzov, Nadav Ahituv, Dhivya Arasappan, Jose Juan Almagro Armenteros, Brian J. Beliveau, Jaroslav Bendl, Sabina Berretta, Rahul A. Bharadwaj, Arjun Bhattacharya, Lucy Bicks, Kristen Brennand, Davide Capauto, Frances A. Champagne, Tanima Chatterjee, Chris Chatzinakos, Yuhang Chen, H. Isaac Chen, Yuyan Cheng, Lijun Cheng, Andrew Chess, Jo-fan Chien, Zhiyuan Chu, Declan Clarke, Ashley Clement, Leonardo Collado-Torres, Gregory M. Cooper, Gregory E. Crawford, Rujia Dai, Nikolaos P. Daskalakis, Jose Davila-Velderrain, Amy Deep-Soboslay, Chengyu Deng, Christopher P. DiPietro, Stella Dracheva, Shiron Drusinsky, Ziheng Duan, Duc Duong, Cagatay Dursun, Nicholas J. Eagles, Jonathan Edelstein, Prashant S. Emani, John F. Fullard, Kiki Galani, Timur Galeev, Michael J. Gandal, Sophia Gaynor, Mark Gerstein, Daniel H. Geschwind, Kiran Girdhar, Fernando S. Goes, William Greenleaf, Jennifer Grundman, Hanmin Guo, Qiuyu Guo, Chirag Gupta, Yoav Hadas, Joachim Hallmayer, Xikun Han, Vahram Haroutunian, Natalie Hawken, Chuan He, Ella Henry, Stephanie C. Hicks, Marcus Ho, Li-Lun Ho, Gabriel E. Hoffman, Yiling Huang, Louise A. Huuki-Myers, Ahyeon Hwang, Thomas M. Hyde, Artemis Iatrou, Fumitaka Inoue, Aarti Jajoo, Matthew Jensen, Lihua Jiang, Peng Jin, Ting Jin, Connor Jops, Alexandre Jourdon, Riki Kawaguchi, Manolis Kellis, Joel E. Kleinman, Steven P. Kleopoulos, Alex Kozlenkov, Arnold Kriegstein, Anshul Kundaje, Soumya Kundu, Cheyu Lee, Donghoon Lee, Junhao Li, Mingfeng Li, Xiao Lin, Shuang Liu, Jason Liu, Jianyin Liu, Chunyu Liu, Shuang Liu, Shaoke Lou, Jacob M. Loupe, Dan Lu, Shaojie Ma, Liang Ma, Michael Margolis, Jessica Mariani, Keri Martinowich, Kristen R. Maynard, Samantha Mazariegos, Ran Meng, Richard M. Myers, Courtney Micallef, Tatiana Mikhailova, Guo-li Ming, Shahin Mohammadi, Emma Monte, Kelsey S. Montgomery, Jill E. Moore, Jennifer R. Moran, Eran A. Mukamel, Angus C. Nairn, Charles B. Nemeroff, Pengyu Ni, Scott Norton, Tomasz Nowakowski, Larsson Omberg, Stephanie C. Page, Saejeong Park, Ashok Patowary, Reenal Pattni, Geo Pertea, Mette A. Peters, Nishigandha Phalke, Dalila Pinto, Milos Pjanic, Sirisha Pochareddy, Katherine S. Pollard, Alex Pollen, Henry Pratt, Pawel F. Przytycki, Carolin Purmann, Zhaohui S. Qin, Ping-Ping Qu, Diana Quintero, Towfique Raj, Ananya S. Rajagopalan, Sarah Reach, Thomas Reimonn, Kerry J. Ressler, Deanna Ross, Panos Roussos, Joel Rozowsky, Misir Ruth, W. Brad Ruzicka, Stephan J. Sanders, Juliane M. Schneider, Soraya Scuderi, Robert Sebra, Nenad Sestan, Nicholas Seyfried, Zhiping Shao, Nicole Shedd, Annie W. Shieh, Joo Heon Shin, Mario Skarica, Clara Snijders, Hongjun Song, Matthew W. State, Jason Stein, Marilyn Steyert, Sivan Subburaju, Thomas Sudhof, Michael Snyder, Ran Tao, Karen Therrien, Li-Huei Tsai, Alexander E. Urban, Flora M. Vaccarino, Harm van Bakel, Daniel Vo, Georgios Voloudakis, Brie Wamsley, Tao Wang, Sidney H. Wang, Daifeng Wang, Yifan Wang, Jonathan Warrell, Yu Wei, Annika K. Weimer, Daniel R. Weinberger, Cindy Wen, Zhiping Weng, Sean Whalen, Kevin P. White, A. Jeremy Willsey, Hyejung Won, Wing Wong, Hao Wu, Feinan Wu, Stefan Wuchty, Dennis Wylie, Siwei Xu, Chloe X. Yap, Biao Zeng, Pan Zhang, Chunling Zhang, Bin Zhang, Jing Zhang, Yanqiong Zhang, Xiao Zhou, Ryan Ziffra, Zane R. Zeier, and Trisha M. Zintel

Science **384** (6698), eadh1938. DOI: 10.1126/science.adh1938

Science (ISSN 1095-9203) is published by the American Association for the Advancement of Science. 1200 New York Avenue NW, Washington, DC 20005. The title *Science* is a registered trademark of AAAS.